Flow Physics Explains Morphological Diversity of Ciliated Organs

Janna C. Nawroth[1,2,†], Feng Ling[1,2,†], Tara Essock-Burns[3], Margaret McFall-Ngai[3,5,6], Kakani Katija[7], Eva Kanso[1*]

[1]Department of Aerospace and Mechanical Engineering, University of Southern California, Los Angeles, California 90089, USA

[2]Helmholtz Pioneer Campus, Helmholtz Munich - Deutsches Forschungszentrum für Gesundheit und Umwelt (GmbH), Ingolstaedter Landstrasse 1, 85764 Neuherberg, Germany

[3] Kewalo Marine Laboratory, University of Hawaii at Manoa, USA

[4] Pacific Biosciences Research Center, University of Hawaii at Manoa, USA

[5] Biology and Environmental Research Division, Carnegie Insitute, California, USA

[6] Monterey Bay Aquarium Research Institute, California, USA

*To whom correspondence should be addressed; E-mail: kanso@usc.edu.

†J.C.N, and F.L. contributed equally to this work.

Ciliated organs that pump luminal fluids are integral to animal physiology. Such organs, including the human airways and reproductive tracts, feature ciliated ducts that direct internal flows. Although cilia organization and duct morphology vary drastically in the animal kingdom, ducts are typically classified into two, seemingly disconnected, archetypes: the familiar carpet and the intriguing flame designs. The reason behind this dichotomy and how duct design relates to fluid pumping remain unclear. Here, we apply morphometric and mechanistic analyses to ciliated ducts across all animal phyla. We find that two structural parameters, lumen diameter and cilia-to-lumen ratio, organize

the observed duct diversity into a continuous spectrum that connects carpets to flames. Using a unified fluid model, we discover that carpets and flames, respectively, maximize flow rate and pressure generation, which is consistent with physiological requirements for bulk transport and filtration, whereas intermediate designs along the morphological spectrum constitute optimally efficient hybrids. We propose that convergence of ciliated organ designs follows functional constraints rather than phylogenetic distance, and we present universal design rules for ciliary pumps.

Introduction

To perform their physiological functions, many organs in animal biology rely on luminal flows driven by the coordinated beat of motile cilia. In humans, ciliated ducts (CDs) pump fluids in the airways [1], brain ventricles and spinal canal [2], and reproductive system [3]. Their failure is directly linked to major pathologies, including bronchiectasis [4], hydrocephalus [5], and ectopic pregnancy [6]. Cilia in these ducts are usually short relative to the lumen diameter and are oriented perpendicular to the epithelial surface, in a ciliary carpet design [7]. Many animals also feature ducts with a strikingly different cilia arrangement, the ciliary flame design [8], where tightly packed, comparatively long cilia beat longitudinally along a narrow lumen. Ciliary flames that are thought to pump fluid for the purpose of excretion provide a model system for studying human kidney disease [9, 10].

Despite the fundamental importance of CDs in animal physiology, functional studies of intact CDs are rare [11, 12], and the relationship between CD morphology and their ability to pump fluid remains largely unexplored. Ciliary flames and carpets have not been compared functionally, nor have other CD morphologies been characterized in relation to these two fundamental designs.

Existing studies have focused on exposed ciliated surfaces and externally ciliated organisms because it is difficult to measure ciliary beat and fluid flow in intact internal ducts. Cilia oscillations, metachronal coordination, and microscale flows have been observed in microdissected *ex-vivo* epithelia [13], engineered *in-vitro* tissues [14, 15], and, more recently, in organ-on-chip models [16, 17]. Additionally, leveraging the remarkable conservation of the ultrastructure of motile cilia among eukaryotes, diverse protist and animal model systems have emerged for probing the functional spectrum of cilia, from locomotion and feeding [18, 19] to symbiotic host-microbe partnerships [20, 21]. External cilia that beat longitudinally in solitary or pairwise configurations, such as in mammalian sperm cells or in the unicellular protozoa *Euglena* and algae *Chlamydomonas*, are often called eukaryotic flagella and drive motility and gait transition in these microorganisms [19, 22–24]. But when longitudinally-beating cilia occur internally in a bundle, such as in planarians, they are labeled as ciliary flames, and are thought to be associated with filtration [8–10].

Despite remarkable progress in understanding the functional diversity of cilia, including the physical mechanisms underlying these functions [25–29], to date, the architecture of intact CDs inside of organisms is yet to be related to their pumping performance. Establishing this connection would elucidate the apparent dichotomy between carpets and flames, inform our understanding of human ciliopathies [30], aid in comparing different internal fluid transport mechanisms in animals [31, 32], and help in assessing the hypothesized roles of CDs in excretion [9, 10] and host-microbe interactions [33].

In this study, we leverage two giant larvaceans (*Bathochordaeus stygius* and *Bathochordaeus mcnutti*) as powerful model systems to study intact CDs. Larvaceans belong to Tunicata (Urochordata), a sister clade of vertebrates, and are an emergent model system for the study of gene regulation, chordate evolution, and development [34]. Giant larvaceans feature a multitude of ciliated ducts with both carpet and flame designs with exceptional optical access [35, 36],

providing uniquely ideal conditions for studying the fundamental properties of cilia-generated flows in intact CDs with direct relevance to other chordates including humans.

To derive universal structure-function relationships, we combined our functional studies in giant larvaceans with an exhaustive review of published CDs in animals, and with physics-based computational models. Specifically, we (i) studied the larvacean system to characterize the morphological features and fluid transport mechanisms in flames versus carpets. We then used these insights to (ii) conduct a morphometric analysis of CDs across all animal phyla and identify a two-dimensional (2D) morphospace that organizes the design of CDs by fluid transport function, and to (iii) explain this structure-function relationship through a unifying physics-based model that links duct morphology to fluid pumping in terms of flow rate and pressure generation. We arrive at a functional assessment of CDs based on morphology that could aid in studying their role in human disease as well as inspire engineering applications [37–39].

Results

Ciliary carpet versus flame duct designs

Microscopic inspection revealed that most ciliated ducts in giant larvaceans, such as in the pharynx, esophagus and gut, exhibit the ciliary carpet design associated with mucus clearance and fluid circulation in humans [40] (Fig. 1A). The ciliary flame design, which is associated with filtration in planarians [9], was found in the giant larvaceans' prominent ciliated funnel (Fig. 1A and S.1), an organ whose function remains obscure [41]. To compare and contrast carpet and flame designs, we measured their structural properties, ciliary activity, and fluid transport velocity in the intact animal. In the carpet-style esophagus, cilia are much shorter than the width of the lumen (ca. 6 μm vs. $100 - 200$ μm, respectively) (Fig. 1B) and they beat at ciliary beat frequencies (CBF) of 20 Hz with a stroke cycle perpendicular to the duct

walls (Fig. 1D). Neighboring cilia coordinate their beat longitudinally along the duct and propel luminal fluid and food particles at flow speeds of up to 50 μm s^{-1} (Fig. 1C, Suppl. Movie 1). The ciliary beat frequency and flow parameters are comparable to those of other ciliary carpets, such as the mammalian airway (Fig. S.2A) and ependymal epithelia [2, 42].

In contrast to the carpet-style esophagus, cilia in the larvacean funnel are longer than the width of the duct lumen (ca. 100 μm versus 55 μm, respectively) and align parallel to the lumen in a densely packed fashion (Fig. 1E and S.1B-D), which is typical of ciliary flames associated with filtration [8, 10]. While the beat kinematics of most ciliary flame systems are unknown, our data suggest that the coordinated motion of the many parallel cilia create periodic waves that travel along the entire length of the 100 μm long larvacean flame (Suppl. Movie 2). These cilia beat at a CBF of up to 60 Hz (Fig. 1g), and generate flow speeds of ca. 40 μm s^{-1} towards the internal blood sinus (Fig. 1F, Suppl. Movie 3). The kinematics of the larvacean ciliary flame are similar to those of the better studied, 20-times shorter ciliary flames of planarians (Fig. S.2B) [43], and appear to be a key feature by which ciliary flames transfer a directional force to the surrounding fluid regardless of flame size.

The stark structural differences between ciliary carpets and flames and the apparent lack of other CD designs in larvaceans underscore the questions of whether all ciliated ducts in nature fall into one of these two design categories and what the functional consequences are.

Comparative morphometric analysis suggests functional constraints on duct designs

To address these questions we performed an exhaustive survey on the presence, morphology, and reported fluid transport functions of CDs in all 34 animal phyla [44, 45]. Since kinematic data of ciliary beat was unavailable in most cases, we collected morphometric data accessible from still images of CDs, namely, cilia orientation relative to duct (perpendicular or longitu-

dinal), duct length L, duct diameter H, cilia length $h/2$, and cilia-to-lumen ratio h/H, which ranges from 0 to 1 and represent the relative fraction of the duct taken up by cilia, independent of cilia orientation (Fig. 2A and Fig. S.3). We collected these data from published work and our own imaging analysis of multiple species of Urochordates and Mollusks (Fig. S.4), covering a total of 58 duct systems representing 26 animal phyla (Table S1). The remaining 8 phyla either lacked evidence of motile cilia or CDs or, in the case of sponges (phylum Porifera), were excluded because of their complex duct morphologies [46, 47].

Using a cross-validated machine learning approach, we probed the ability of the morphometric parameters to correctly predict whether a given ciliated duct was reported to perform bulk transport (clearance, circulation, or cargo transport) or serve as a filter/valve. We found that the cilia-to-lumen ratio h/H was a perfect predictor of known CD function and, when plotted against lumen diameter H to visualize the spatial scales involved, organized the 58 surveyed duct systems by function (Fig. 2B and Fig. S.5). A value of h/H >0.62 was associated with filtration or valve function, and a value of h/H <0.62 indicated bulk fluid transport Mapping cilia orientation onto the morphometric distribution further showed a clear association of filtration/valve function with flame designs (longitudinal cilia and high values of h/H) and of bulk transport with carpet designs (perpendicular cilia and low values of h/H). Cilia orientation by itself was not an optimal predictor of function due to marked exceptions, such as longitudinally aligned (but sparse) cilia in the collecting ducts of planarian excretory organs, which perform bulk transport of fluid [8]. Other morphometric parameters, e.g., duct length or diameter, were at best weakly predictive of CD function (Fig. S.6).

The h/H against H plot showed a continuous distribution of designs spanning carpets to flames, rather than a strict dichotomy. CD designs can thus be described by their unique combination of cilia-to-lumen ratio and lumen diameter. In general, higher cilia-to-lumen ratios tended to associate with narrower ducts and flame designs, and lower cilia-to-lumen ratios with

wider ducts and carpet designs, whereas systems with large H and large h/H, for example, were markedly absent. Importantly, the data associated with filtration and transport functions separated into two power laws: for transport (circles), $h \propto H^{0.4}$ while for filtration (triangles), $h \propto H$ (inset Fig. 2A). The cases with unknown function (squares) spanned both trends. Mapping the two power laws onto the morphospace $(h/H, H)$ (dashed lines, Fig. 2A) emphasized the strong correlation between the fluid function – filtration or transport – and the ciliated duct morphology. As the distribution of systems in the morphospace was not reflected by their phylogenetic distance (Fig. 2 and S.5) but organized by their fluid transport activity, these data suggest a convergent evolution of CD designs based on function.

Intuitively, the design of CDs for fluid pumping is constrained by the metabolic cost of building and actuating the cilia [48, 49], limiting the number and length of cilia on a given ciliated surface. A higher cilia-to-lumen ratio h/H also implies that less space in the duct lumen can be taken up by fluid. Minimizing the cost of cilia production along a cell surface and the cost of cilia activity while maximizing fluid volume seems to favor a low cilia-to-lumen ratio at large lumen diameter. However, the flame cells observed in purported filtration systems suggest that other functional considerations are at play. Specifically, structural data suggest that flame cells achieve filtration by pumping fluid through a flow-resisting sieve [8, 50, 51], indicating that higher cilia-to-lumen ratios may be specialized to pump fluid in the presence of high resistance to flow, or, equivalently, in the presence of *adverse pressure gradients* that cause counter-currents relative to the desired flow direction.

We hypothesized that lower cilia-to-lumen ratios which transport fluids at comparatively greater lumen diameters and flow rates, are able to pump flows at low or zero adverse pressures, whereas higher cilia-to-lumen ratios are limited to small diameters and low flow rates because of the high density of active ciliary material required to overcome adverse pressure gradients. These trade-offs would explain both the non-uniform distribution of CD designs and

their functional classification.

A unified model of fluid transport in ciliated duct designs

To rigorously probe this hypothesis, we used a Brinkman-Stokes model, where a cylindrical duct of diameter H is lined by a porous layer of overall thickness h representing the ciliary layer, enclosing an inner free lumen of diameter $(H - h)$ (Fig. 3 and Suppl. Methods §S.2). This lumped-layer model emulates ciliary carpets for h small relative to H and resembles ciliary flames as h approaches H. It thus bridges the two archetypes, carpets and flames, in a concise way that is unachievable using existing envelope [13, 52–56] and discrete cilia models [25, 57–63] and enables efficient exploration of the entire morphospace spanned by h/H and H independent of cilia orientation, including designs not (yet) known to biology.

In the model, all characteristics of the ciliary layer were subsumed into three parameters: a cilia fraction φ_c and its complementary fluid fraction $\varphi = 1 - \varphi_c$, a uniform force density f_c exerted by the cilia on the fluid (or the pressure gradient generated by ciliary force in a pipe [64]), and an effective Brinkman coefficient K_c encoding the drag resistance to fluid flows due to the presence of the cilia. This generic representation captures the two salient features of the ciliary layer – the cilia-generated force and drag-induced resistance to fluid flows – irrespective of the details of cilia distribution and beat kinematics.

In ciliary carpets, because cilia are mainly orthogonal to the duct surface, the cilia fraction φ_c can be estimated from longitudinal cross-sections of the duct, looking down at the density of cilia on the surface. Available images and our own data show little variations in φ_c across ciliary carpets for small h/H; we thus set $\lim_{h/H \to 0} \varphi_c = 0.1$ (Suppl. Methods §S.3). In the flame systems, because cilia are mainly parallel to the duct wall, φ_c is determined by taking transverse cross-sections, and, by definition, is proportional to the cilia-to-lumen ratio h/H constructed from surveyed images. These observations inspire an empirical nonlinear fit of φ_c

as a function of h/H that spans carpet and flame designs (Fig. 3E).

More cilia generate more force. By linearity of the dilute resistive-force theory in the Brinkman model, the ciliary force density f_c must scale linearly with the cilia fraction φ_c. The fluid fraction φ is also important to transfer the ciliary force to the surrounding fluid; letting f_c be proportional to φ avoids the nonphysical situation of generating a ciliary force when $\varphi = 0$. We thus set $f_c = f\varphi_c\varphi$, with a constant force density coefficient f. Meanwhile, more cilia induce higher resistance to fluid flows in the ciliary layer, and, by the same linearity argument, the effective Brinkman coefficient $K_c = \kappa\varphi_c$ must be proportional to φ_c, where κ is a proportionality constant.

The downstream fluid velocities u_z^c and u_z^l in the ciliary and free lumen layers are, by axisymmetry, function of the radial distance r only and are governed by the Brinkman and Stokes equations, respectively, with proper boundary conditions (BCs),

$$\begin{aligned}
&\text{Cilia layer:} && \mu\frac{1}{r}\frac{\partial}{\partial r}\left[r\frac{\partial}{\partial r}u_z^c\right] = \varphi\frac{\mathrm{d}p}{\mathrm{d}z} + K_c u_z^c + f_c, \\
&\text{Lumen layer:} && \mu\frac{1}{r}\frac{\partial}{\partial r}\left[r\frac{\partial u_z^l}{\partial r}\right] = \frac{\mathrm{d}p}{\mathrm{d}z}, \\
&\text{BCs:} && r = 0: \quad u_z^l \text{ finite}, \qquad r = H: \quad u_z^c = 0, \\
& && r = (H-h)/2: \quad \varphi u_z^c = u_z^l, \quad \sigma_{rz}^c = \varphi\sigma_{rz}^l.
\end{aligned} \tag{1}$$

Here, μ denotes the fluid viscosity, $\mathrm{d}p/\mathrm{d}z$ the adverse pressure gradient, and $\sigma_{rz}^{(\cdot)} = \mu\partial u_z^{(\cdot)}/\partial r$ the fluid shear stress [65, 66]; see Suppl. Methods §S.2 for analytical solutions to (1).

For constant cilia fraction φ_c, the profile of the fluid velocity $u_z(r)$, equal to u_z^l in the free lumen layer and φu_z^c in the ciliary layer, decreased with increasing Brinkman resistance κ and increased with increasing cilia forcing f and cilia-to-lumen ratio h/H (Fig. 3B-C). Importantly, in the presence of adverse pressure dp/dz ducts with low cilia-to-lumen ratio failed and allowed reversal of luminal flow, whereas positive luminal flow remained robust at high cilia-to-lumen

ratio (Fig. 3D).

Considering the best fit of φ_c to experimental data (Fig. 3E), the corresponding ciliated area $A_c = \int \varphi_c \mathrm{d}A$ varied over the morphospace $(H, h/H)$ (Fig. 3F). We computed the associated net flows $U_z = \int u_z \mathrm{d}A$ for all $(H, h/H)$ at zero and non-zero adverse pressure (Fig. 3G). At $dP/dz = 0$, any CD design in the morphospace $(H, h/H)$ can produce positive flow; however, speed decreased with increasing cilia-to-lumen ratio h/H for a given lumen diameter H.

This trade-off between maximizing net flows versus sustaining an adverse pressure is best appreciated in the pump function space $(Q, \mathrm{d}p/\mathrm{d}z)$, where $Q = \int U_z \mathrm{d}A$ is the net flow rate (Fig. 4A). Each CD operates along its own characteristic curve, connecting its maximal generated flow rate Q at $\mathrm{d}p/\mathrm{d}z = 0$ to the maximal adverse pressure $\mathrm{d}p/\mathrm{d}z$ sustained without causing flow reversal $Q = 0$ as depicted in Fig. 4A, with solid pink lines corresponding to the $(H, h/H)$ values of larvacean ducts in Fig. 1. Intuitively, a CD performs best when operating near the transition from maximal flow rate to maximal pressure.

Optimal duct design depends on pressure requirements

To systematically probe optimal CD designs, we introduced a pumping efficiency $E = Q/A_c$ defined as the ratio of the volumetric flow rate Q to total ciliary material A_c per cross sectional area. We sought optimal geometries $(H, h/H)$ that maximize E under an imposed adverse pressure gradient $\mathrm{d}p/\mathrm{d}z$.

For a given $\mathrm{d}p/\mathrm{d}z$, we computed the flow speed U_z over the entire morphospace $(H, h/H)$. At each $(H, h/H)$, we calculated Q and E and identified the duct design $(H, h/H)$ that maximized E. We assessed the performance of each $(H, h/H)$ relative to the optimal design by computing its relative pumping efficiency E_{rel} scaled by the maximal pumping efficiency value. We repeated this process for a range of $\mathrm{d}p/\mathrm{d}z \in [10^{-10}, 10^{2}]$ [Pa/μm], and obtained the most efficient design values of $(H, h/H)$ as a function of $\mathrm{d}p/\mathrm{d}z$; see also Suppl. Methods, Algo-

rithm S.1. Optimization results are plotted on the function space $(Q, \mathrm{d}p/\mathrm{d}z)$ (Fig. 4A, solid grey line). Results using the experimental values of $(H, h/H)$ from Fig. 2A in our fluid model are superimposed (colored markers). The model predicts that the empirical ducts follow the optimal trend, with transport systems (circles) exhibiting larger Q values at lower $\mathrm{d}p/\mathrm{d}z$ and filtrations systems (triangles) larger $\mathrm{d}p/\mathrm{d}z$ at lower Q, and systems with unknown functions spanning both.

We plotted the optimal duct designs on the morphospace $(H, h/H)$ (Fig. 4B, solid white line) and depicted the highest relative efficiency E_{rel} as a colormap over the entire morphospace, which excludes designs both in the small H, low h/H and in the large H, high h/H corners of the morphospace. Designs that have relatively small lumen diameter H and low cilia-to-lumen ratio h/H are sub-optimal because for the same $\mathrm{d}p/\mathrm{d}z$, ducts with larger H are always more efficient in transporting flows (Fig. 4A, dotted grey lines). Designs that have relatively large H and high h/H are also sub-optimal because increasing the lumen diameter H limits the value of $\mathrm{d}p/\mathrm{d}z$ that can be sustained at high h/H. Additionally, when increasing H at high h/H, the required ciliary material also grows, likely beyond biological limits.

Superimposing the biological data onto Fig. 4B, all surveyed designs closely aligned with the line that maximizes pumping efficiency. Importantly, systems with presumed filtration functions are typically ciliary flames and occupy the region of the morphospace with smaller lumen diameter H and higher cilia-to-lumen ratio h/H. This zone is characterized by its ability to sustain higher maximum adverse pressure gradient just before flow reverses ($U_z = Q = 0$); see Fig. 4C. Conversely, systems whose primary function is to transport luminal fluid in bulk are typically ciliary carpets and thus reside in the region of the morphospace with larger lumen diameter H and lower cilia-to-lumen ratio h/H, a zone characterized by its ability to produce higher maximum flow rates (Fig.4D).

Discussion

We established a quantitative link between the morphology and fluid pumping function of ciliated organs. Our analyses imply that the distribution of morphological features of ciliated ducts in nature is not accidental since each biological system in our survey is the optimal pump for operation at a specific pressure and flow rate. At the extreme ends of the spectrum, systems with cilia-to-lumen ratios near zero maximize flow rate whereas systems with cilia-to-lumen ratios near unity optimize pressure generation, consistent with the known roles of ciliary carpets in bulk transport and of flame cells in ultrafiltration, respectively. Notably, our study reveals that many systems exhibit intermediate cilia-to-lumen ratios and predicts that they may perform fluid transport against some resistance, for example, to maintain a hydrostatic head [67]. Our analysis also explains the absence of surveyed CDs in two quadrants of the morphospace because our model predicts such pump designs to be either comparatively inefficient, e.g., the same flow rate would be possible at less power input, or unfeasible given likely biological limits on ciliary material and power input.

Given such morphology dependent fine-tuning of pump performance, we can now use structural features of a given CD to predict its relative ability to either transport fluids in bulk or to perform filtration. Case in point, our findings support the decades-old hypothesis that the larvacean's ciliated funnel (Fig. 1, Fig. 2a and Suppl. Movie 2) helps maintain the internal fluid volume through unidirectional injection of filtered seawater into the blood [68], rather than being limited to sensory and endocrine functions [41, 69, 70]. In the Hawaiian bobtail squid (*Euprymna scolopes*), we can predict that the ciliated conduit to the light organ that hosts the bacterial symbiont (*Vibrio fischeri*) transports fluids in the duct and antechamber, whereas filtration or pressurization may occur in the bottleneck region (Fig. S.4C-E). Importantly, the bottleneck diameter varies dynamically during different stages of colonization [33], suggesting a

switch between filtration and clearance functions that could help maintain the host-symbiont association. Similarly, the ciliated pore canals of the madreporite in sea urchins appear to change dynamically between low and high cilia-to-lumen ratios (Suppl. Table 1), and our results support the proposed functional switch between fluid pump and valve that maintains the animal's inner hydrostatic pressure [67].

Our findings may provide general insights into the evolution of waste excretion strategies in animals and offer a functional explanation why ciliary flame-based excretory organs are abundant in animals not exceeding a few milligrams in body mass, whereas larger animals rely on blood pressure pumped by the muscle-powered heart [71]. Our study suggests two mechanisms. First, assuming cilia have limited length and emanate at finite density from the tissue surface, increasing the lumen diameter eventually lowers the cilia-to-lumen ratio and restricts the active force density, thus limiting the pressure that can be sustained and the flow rate than can be generated by an individual flame pump. Second, scaling up flame-based filtration by the parallel operation of many small flame units would require a much larger organ volume than a system that leverages the higher filtration fluid pressures achieved by the heart (Suppl. Methods §S.4). But even if we were to assume unlimited cilia length and lumen diameter, advantageous scaling of energy efficiency in muscle versus ciliated cells could disfavor the emergence of extremely long ciliated flames and bias evolution towards muscle-powered pumps in larger animals.

Along with assessing the pumping function of healthy ciliated organs, our study may aid in the functional interpretation of disease phenotypes, such as narrowing of ciliated ducts [72], and inform the development of drugs that disrupt excretory functions of parasites [43]. Additionally, our approach provides a rational design tool for tissue-engineered and synthetic ciliary pumps and devices that perform filtration and flow control, in addition to existing carpet-like configurations for bulk transport [37–39, 73].

Our analysis does have limitations. Our survey might be missing alternative CD designs in

the "hidden biology" of less studied animals [74]. We also omitted ciliated ducts whose geometry is not well described by our 2D morphospace, such as the ciliated chamber of sponges [46, 47, 75] and some of the unique ciliated spaces found in ctenophores [76–79]. No distinction was made between different types of fluids, such as mucus and water, and we did not consider mixing flows. We considered a Newtonian fluid model and fundamental measures of pumping performance in order to limit the number of variables and reveal the dominant structure-function relationships of ciliated ducts. Our model robustly captures leading order effects of ciliary fluid pumping without requiring implementation of detailed cilia kinematics. Hence, limitations notwithstanding, our 2D morphospace and functional map are representative and relevant for the majority of ciliated ducts known to biology and provide a universal tool for assessing the physiological role and integrity of ciliated organs.

Funding

This work was funded by NSF Inspire grant MCB1608744 (E.K. and M.M.-N.), NIH R01 HL153622 grant (E.K. and J.N.), NIH R37 AI50661, COBRE P20 GM125508, OD11024 and GM135254 grants (M.M.-N.), DMR-2004469 (M.J.S.), and David & Lucile Packard Foundation (K.K.). Acquisition of the Leica TCS SP8 X confocal microscope was supported by NSF DBI 1828262 (M.M.-N.).

Authors contributions

Janna Nawroth: Conceptualization, Investigation, Methodology, Formal Analysis, Software, Data curation, Writing- Original draft preparation, Reviewing and Editing. Feng Ling: Investigation, Methodology, Formal Analysis, Software, Data curation, Validation, Visualization, Writing- Original draft preparation, Reviewing and Editing. Tara Essock-Burns: Investigation, Visualization, Writing - Reviewing and Editing. Margaret McFall-Ngai: Writing - Review-

ing and Editing, Funding acquisition. Kakani Katija: Methodology, Investigation, Resources, Writing - Reviewing and Editing. Eva Kanso: Conceptualization, Investigation, Methodology, Formal Analysis, Writing- Original draft preparation, Reviewing and Editing, Supervision, Funding acquisition.

Competing interests

The authors declare no competing interests.

Data and materials availability

All data is available in the manuscript or the supplementary materials.

Materials and Methods

Experimental methods. We collected four different larvacean species (*Bathochordaeus mcnutti, Bathochordaeus stygius, Fritillaria sp., Mesochordaeus erythrocephala*) and conducted in situ high-speed video microscopy of intact internal ciliated ducts to capture ciliary beat kinematics and fluid transport [20]. We also reanalyzed ciliary beat videos we previously recorded in human airway epithelial cultures [80]. To measure ciliated duct morphology, we employed immunofluorescence (IF) imaging of fixed samples of larvaceans and the Hawaiian bobtail squid (*Euprymna scolopes*). Additionally, we collected and analyzed CD morphology from micrographs in literature representing all animal phyla, exclusions applied. The morphometric data sets were analyzed using machine learning to identify the structural parameters most predictive of fluid transport functions (bulk transport or filtration/valving) reported in literature. Complete methods for data acquisition and analysis are provided in Suppl. Materials § S.1

References

1. Bustamante-Marin, X. M. & Ostrowski, L. E. Cilia and mucociliary clearance. *Cold Spring Harbor Perspectives in Biology* **9,** a028241 (2017).
2. Faubel, R., Westendorf, C., Bodenschatz, E. & Eichele, G. Cilia-based flow network in the brain ventricles. *Science* **353,** 176–178 (2016).
3. Raidt, J. *et al.* Ciliary function and motor protein composition of human fallopian tubes. *Human Reproduction* **30,** 2871–2880 (2015).
4. Tilley, A. E., Walters, M. S., Shaykhiev, R. & Crystal, R. G. Cilia dysfunction in lung disease. *Annual Review of Physiology* **77,** 379–406 (2015).
5. Carter, C. S. *et al.* Abnormal development of NG2+ PDGFR-α+ neural progenitor cells leads to neonatal hydrocephalus in a ciliopathy mouse model. *Nature Medicine* **18,** 1797–1804 (2012).
6. Blyth, M. & Wellesley, D. Ectopic pregnancy in primary ciliary dyskinesia. *Journal of Obstetrics and Gynaecology* **28,** 358–358 (2008).
7. Gilpin, W., Bull, M. S. & Prakash, M. The multiscale physics of cilia and flagella. *Nature Reviews Physics* **2,** 74–88 (2020).
8. McKanna, J. A. Fine structure of the protonephridial system in Planaria. *Zeitschrift für Zellforschung und Mikroskopische Anatomie* **92,** 509–523 (1968).
9. Rink, J. C., Vu, H. T.-K. & Alvarado, A. S. The maintenance and regeneration of the planarian excretory system are regulated by EGFR signaling. *Development* **138,** 3769–3780 (2011).
10. Vu, H. T.-K. *et al.* Stem cells and fluid flow drive cyst formation in an invertebrate excretory organ. *eLife* **4,** e07405 (2015).
11. Vogel, S. Living in a physical world X. Pumping fluids through conduits. *Journal of biosciences* **32,** 207–222 (2007).
12. Yuan, S. *et al.* Motile cilia of the male reproductive system require miR-34/miR-449 for development and function to generate luminal turbulence. *Proceedings of the National Academy of Sciences* **116,** 3584–3593 (2019).
13. Ramirez-San Juan, G. R. *et al.* Multi-scale spatial heterogeneity enhances particle clearance in airway ciliary arrays. *Nature Physics* **16,** 1–7 (2020).
14. Pellicciotta, N. *et al.* Cilia density and flow velocity affect alignment of motile cilia from brain cells. *Journal of Experimental Biology* **223** (2020).
15. Pellicciotta, N. *et al.* Entrainment of mammalian motile cilia in the brain with hydrodynamic forces. *Proceedings of the National Academy of Sciences* **117,** 8315–8325. ISSN: 0027-8424 (2020).

16. Nawroth, J. C. *et al.* A microengineered airway lung chip models key features of viral-induced exacerbation of asthma. *American Journal of Respiratory Cell and Molecular Biology* **63,** 591–600 (2020).

17. Sone, N. *et al.* Multicellular modeling of ciliopathy by combining iPS cells and microfluidic airway-on-a-chip technology. *Science Translational Medicine* **13** (2021).

18. Solari, C. A., Ganguly, S., Kessler, J. O., Michod, R. E. & Goldstein, R. E. Multicellularity and the functional interdependence of motility and molecular transport. *Proceedings of the National Academy of Sciences* **103,** 1353–1358 (2006).

19. Wan, K. Y. & Goldstein, R. E. Coordinated beating of algal flagella is mediated by basal coupling. *Proceedings of the National Academy of Sciences* **113,** E2784–e2793 (2016).

20. Nawroth, J. C. *et al.* Motile cilia create fluid-mechanical microhabitats for the active recruitment of the host microbiome. *Proceedings of the National Academy of Sciences* **114,** 9510–9516 (2017).

21. Kanso, E. A., Lopes, R. M., Strickler, J. R., Dabiri, J. O. & Costello, J. H. Teamwork in the viscous oceanic microscale. *Proceedings of the National Academy of Sciences* **118.** ISSN: 0027-8424 (2021).

22. Guo, H., Fauci, L., Shelley, M. J. & Kanso, E. Bistability in the synchronization of actuated microfilaments. *Journal of Fluid Mechanics* **836,** 304–323 (2018).

23. Man, Y. & Kanso, E. Multisynchrony in active microfilaments. *Physical Review Letters* **125,** 148101 (2020).

24. Guo, H., Man, Y., Wan, K. Y. & Kanso, E. Intracellular coupling modulates biflagellar synchrony. *Journal of the Royal Society Interface* **18,** 20200660 (2021).

25. Ding, Y., Nawroth, J. C., McFall-Ngai, M. J. & Kanso, E. Mixing and transport by ciliary carpets: a numerical study. *Journal of Fluid Mechanics* **743,** 124–140 (2014).

26. Elgeti, J. & Gompper, G. Emergence of metachronal waves in cilia arrays. *Proceedings of the National Academy of Sciences* **110,** 4470–4475 (2013).

27. Chateau, S., Favier, J., Poncet, S. & d'Ortona, U. Why antiplectic metachronal cilia waves are optimal to transport bronchial mucus. *Physical Review E* **100,** 042405 (2019).

28. Meng, F., Bennett, R. R., Uchida, N. & Golestanian, R. Conditions for metachronal coordination in arrays of model cilia. *Proceedings of the National Academy of Sciences* **118** (2021).

29. Kanale, A. V., Ling, F., Guo, H., Fürthauer, S. & Kanso, E. Spontaneous phase coordination and fluid pumping in model ciliary carpets. *Proceedings of the National Academy of Sciences* **119,** e2214413119 (2022).

30. Hildebrandt, F., Benzing, T. & Katsanis, N. Ciliopathies. *New England Journal of Medicine* **364,** 1533–1543 (2011).

31. Andrikou, C., Thiel, D., Ruiz-Santiesteban, J. A. & Hejnol, A. Active mode of excretion across digestive tissues predates the origin of excretory organs. *PLOS Biology* **17,** e3000408 (2019).

32. Ichimura, K. & Sakai, T. Evolutionary morphology of podocytes and primary urine-producing apparatus. *Anatomical Science International* **92,** 161–172 (2017).

33. Essock-Burns, T., Bongrand, C., Goldman, W. E., Ruby, E. G. & McFall-Ngai, M. J. Interactions of Symbiotic Partners Drive the Development of a Complex Biogeography in the Squid-Vibrio Symbiosis. *mBio* **11** (2020).

34. Glover, J. C. Oikopleura. *Current Biology* **30,** R1243–r1245 (2020).

35. Sherlock, R., Walz, K., Schlining, K. & Robison, B. Morphology, ecology, and molecular biology of a new species of giant larvacean in the eastern North Pacific: Bathochordaeus mcnutti sp. nov. *Marine Biology* **164,** 20 (2017).

36. Katija, K. *et al.* Revealing enigmatic mucus structures in the deep sea using DeepPIV. *Nature* **583,** 78–82 (2020).

37. Yang, Z. & Zhang, L. Magnetic actuation systems for miniature robots: A review. *Advanced Intelligent Systems* **2,** 2000082 (2020).

38. Zhang, R., den Toonder, J. & Onck, P. R. Transport and mixing by metachronal waves in nonreciprocal soft robotic pneumatic artificial cilia at low Reynolds numbers. *Physics of Fluids* **33,** 092009 (2021).

39. Islam, T. U. *et al.* Microscopic artificial cilia-a review. *Lab on a Chip* (2022).

40. Meunier, A. & Azimzadeh, J. Multiciliated cells in animals. *Cold Spring Harbor Perspectives in Biology* **8,** a028233 (2016).

41. Holmberg, K. The ciliated brain duct of Oikopleura dioica (Tunicata, Appendicularia). *Acta Zoologica* **63,** 101–109 (1982).

42. Sears, P. R., Yin, W.-N. & Ostrowski, L. E. Continuous mucociliary transport by primary human airway epithelial cells in vitro. *American Journal of Physiology-Lung Cellular and Molecular Physiology* **309,** L99–l108 (2015).

43. Valverde-Islas, L. E. *et al.* Visualization and 3D reconstruction of flame cells of Taenia solium (cestoda). *PLOS One* **6,** e14754 (2011).

44. Dunn, C. W., Giribet, G., Edgecombe, G. D. & Hejnol, A. Animal phylogeny and its evolutionary implications. *Annual Review of Ecology, Evolution, and Systematics* **45,** 371–395 (2014).

45. Feuda, R. *et al.* Improved modeling of compositional heterogeneity supports sponges as sister to all other animals. *Current Biology* **27,** 3864–3870 (2017).

46. Asadzadeh, S. S., Larsen, P. S., Riisgård, H. U. & Walther, J. H. Hydrodynamics of the leucon sponge pump. *Journal of the Royal Society Interface* **16,** 20180630 (2019).

47. Leys, S. P. *et al.* The sponge pump: the role of current induced flow in the design of the sponge body plan. *PLOS One* **6,** e27787 (2011).

48. Marshall, W. F., Qin, H., Brenni, M. R. & Rosenbaum, J. L. Flagellar length control system: testing a simple model based on intraflagellar transport and turnover. *Molecular Biology of the Cell* **16,** 270–278 (2005).

49. Ishikawa, H. & Marshall, W. F. Ciliogenesis: building the cell's antenna. *Nature Reviews Molecular Cell Biology* **12,** 222–234 (2011).

50. Scimone, M. L., Srivastava, M., Bell, G. W. & Reddien, P. W. A regulatory program for excretory system regeneration in planarians. *Development* **138,** 4387–4398 (2011).

51. Ruppert, E. E. & Smith, P. R. The functional organization of filtration nephridia. *Biological Reviews* **63,** 231–258 (1988).

52. Taylor, G. Analysis of the swimming of microscopic organisms. *Proceedings of the Royal Society of London. Series A* **209,** 447–461 (1951).

53. Blake, J. Infinite models for ciliary propulsion. *Journal of Fluid Mechanics* **49,** 209–222 (1971).

54. Pak, O. S., Normand, T. & Lauga, E. Pumping by flapping in a viscoelastic fluid. *Physical Review E* **81,** 036312 (2010).

55. Michelin, S. & Lauga, E. Optimal feeding is optimal swimming for all Péclet numbers. *Physics of Fluids* **23,** 101901 (2011).

56. Chrispell, J. C., Fauci, L. J. & Shelley, M. An actuated elastic sheet interacting with passive and active structures in a viscoelastic fluid. *Physics of Fluids* **25,** 013103 (2013).

57. Liron, N. & Mochon, S. The discrete-cilia approach to propulsion of ciliated microorganisms. *Journal of Fluid Mechanics* **75,** 593–607 (1976).

58. Liron, N. Fluid transport by cilia between parallel plates. *Journal of Fluid Mechanics* **86,** 705–726 (1978).

59. Gueron, S. & Liron, N. Ciliary motion modeling, and dynamic multicilia interactions. *Biophysical Journal* **63,** 1045 (1992).

60. Blake, J., Liron, N. & Aldis, G. Flow patterns around ciliated microorganisms and in ciliated ducts. *Journal of Theoretical Biology* **98,** 127–141 (1982).

61. Ding, Y. & Kanso, E. Selective particle capture by asynchronously beating cilia. *Physics of Fluids* **27,** 121902 (2015).

62. Guo, H. & Kanso, E. Evaluating efficiency and robustness in cilia design. *Physical Review E* **93,** 033119 (2016).

63. Guo, H., Zhu, H. & Veerapaneni, S. Simulating cilia-driven mixing and transport in complex geometries. *Physical Review Fluids* **5,** 053103 (2020).

64. Liron, N. & Shahar, R. Stokes flow due to a Stokeslet in a pipe. *Journal of Fluid Mechanics* **86,** 727–744 (1978).

65. Hou, J. S., Holmes, M. H., Lai, W. M. & Mow, V. C. Boundary Conditions at the Cartilage-Synovial Fluid Interface for Joint Lubrication and Theoretical Verifications. *Journal of Biomechanical Engineering* **111,** 78–87. ISSN: 0148-0731. https://doi.org/10.1115/1.3168343 (Feb. 1989).

66. Damiano, E., Duling, B., Ley, K. & Skalak, T. Axisymmetric pressure-driven flow of rigid pellets through a cylindrical tube lined with a deformable porous wall layer. *Journal of Fluid Mechanics* **314,** 163–189 (1996).

67. Tamori, M., Matsuno, A. & Takahashi, K. Structure and function of the pore canals of the sea urchin madreporite. *Philosophical Transactions of the Royal Society of London. Series B: Biological Sciences* **351,** 659–676 (1996).

68. Ruppert, E. E. Structure, ultrastructure and function of the neural gland complex of Ascidia interrupta (Chordata, Ascidiacea): clarification of hypotheses regarding the evolution of the vertebrate anterior pituitary. *Acta Zoologica* **71,** 135–149 (1990).

69. Bassham, S. & Postlethwait, J. H. The evolutionary history of placodes: a molecular genetic investigation of the larvacean urochordate Oikopleura dioica. *Development* **132,** 4259–4272 (2005).

70. Deyts, C., Casane, D., Vernier, P., Bourrat, F. & Joly, J.-S. Morphological and gene expression similarities suggest that the ascidian neural gland may be osmoregulatory and homologous to vertebrate peri-ventricular organs. *European Journal of Neuroscience* **24,** 2299–2308 (2006).

71. Bartolomaeus, T. & Ax, P. Protonephridia and Metanephridia-their relation within the Bilateria. *Journal of Zoological Systematics and Evolutionary Research* **30,** 21–45 (1992).

72. Ott, E. *et al.* Pronephric tubule morphogenesis in zebrafish depends on Mnx mediated repression of irx1b within the intermediate mesoderm. *Developmental Biology* **411,** 101–114 (2016).

73. Chen, D. & Zhong, Y. A computational model of dynein activation patterns that can explain nodal cilia rotation. *Biophysical Journal* **109,** 35–48 (2015).

74. Dunn, C. W., Leys, S. P. & Haddock, S. H. The hidden biology of sponges and ctenophores. *Trends in Ecology & Evolution* **30,** 282–291 (2015).

75. Leys, S. P. & Eerkes-Medrano, D. I. Feeding in a calcareous sponge: particle uptake by pseudopodia. *The Biological Bulletin* **211,** 157–171 (2006).

76. Norekian, T. P. & Moroz, L. L. Neural System and Receptor Diversity in the ctenophore Beroe abyssicola. *Journal of Comparative Neurology* **527,** 1986–2008 (2019).

77. Tamm, S. L. Cilia and the life of ctenophores. *Invertebrate Biology* **133,** 1–46 (Jan. 2014).

78. Gemmill, J. F. Ciliary action in the internal cavities of the ctenophore Pleurobrachia pileus Fabr. *Proceedings of the Zoological Society of London* **88,** 263–265 (1918).

79. Presnell, J. S. *et al.* The presence of a functionally tripartite through-gut in Ctenophora has implications for metazoan character trait evolution. *Current Biology* **26,** 2814–2820 (2016).

80. Nawroth, J. C., van der Does, A. M., Ryan, A. & Kanso, E. Multiscale mechanics of mucociliary clearance in the lung. *Philosophical Transactions of the Royal Society B* **375,** 20190160 (2020).

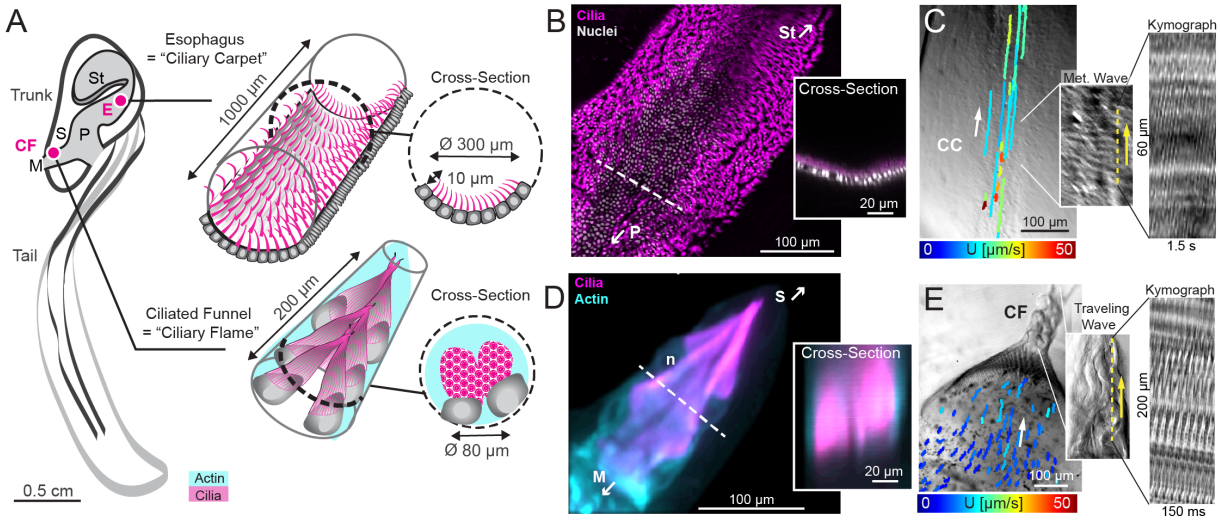

Figure 1: **Comparison of CDs with ciliary flame versus ciliary carpet design in *B. mcnutti* A.** The stomach (St), pharynx (P), and esophagus (E) are lined with ciliary carpets. A ciliated funnel (CF) containing ciliary flame cells connects the mouth (M) cavity to the internal blood sinus (S). **B.** Confocal image of the ciliary carpet of the esophagus (magenta: acetylated α-tubulin). Inset: Horizontal cross section at dotted line. Note that the cilia only fill a small fraction of the lumen. **C.** Direction and magnitude of fluid flow driven by the esophageal ciliary carpet. Insets: Snapshot and kymograph of the esophageal carpet showing metachronal wave and beat frequency of $\sim$20 Hz. Yellow arrow indicates direction of metachronal wave. **D.** Confocal image of the ciliary flame inside the ciliated funnel (magenta: acetylated α-tubulin). Inset: Horizontal cross section at dotted line. Note that the cilia fill a large fraction of the lumen. **E.** Direction and speed of fluid flow converging into the ciliated funnel driven by the ciliary flame. Insets: Snapshot and kymograph of the ciliary flame showing traveling wave and beat frequency of $\sim$60 Hz. Yellow arrow indicates direction of traveling wave.

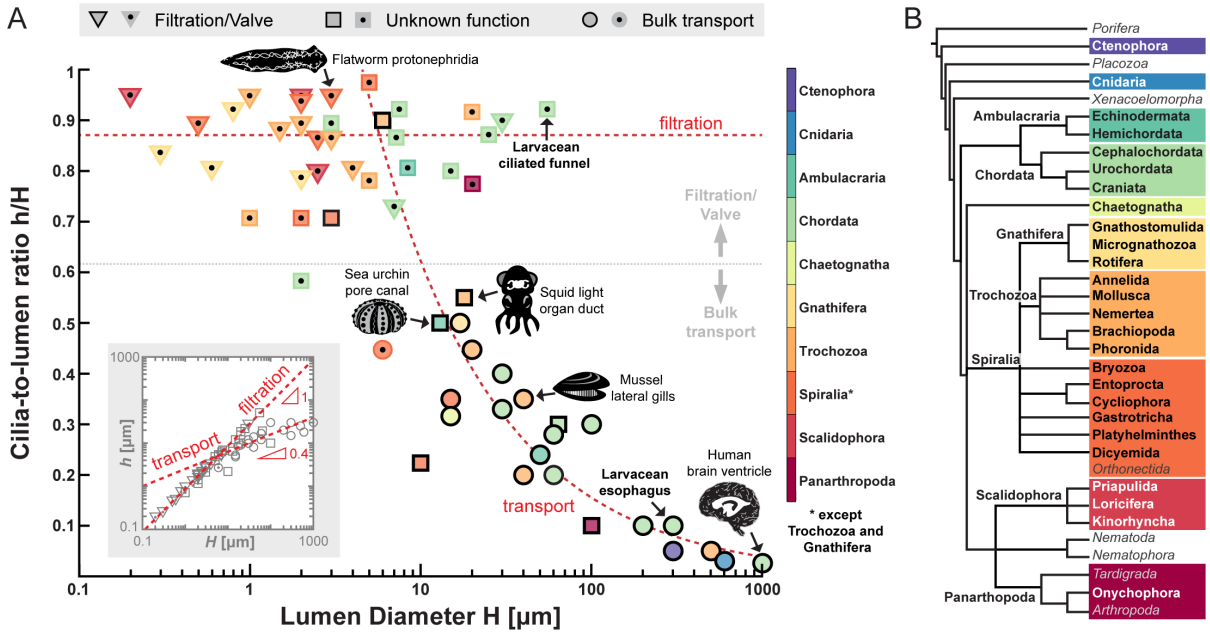

Figure 2: **The morphospace of CDs in nature. A.** CDs plotted based on cilia-to-lumen ratio h/H and lumen diameter H and classified by their functions and phyla (also see Fig. S.5). Triangles ▽ represent systems whose primary functions are thought to be (ultra-) filtration, excretion, or pressure generation. Circles ○ denote systems that transport or mix food particles, liquids, or cells. Squares □ represent systems whose fluid transport functions are currently unknown or disputed. Symbols with solid boundaries are systems with perpendicular ciliation and symbols with a central dot are systems with longitudinal ciliation. The color code indicates the phylogenetic clades listed in the color bar. The dotted grey line indicates the h/H value identified by machine learning to divide systems with filtration function from systems with bulk transport function. The two red dashed lines correspond to the power-law fit for systems with bulk transport and filtration functions, respectively, shown in the inset. **B.** Phylogenetic tree showing the phyla known to feature CDs and included in the analysis (bold type) and the phyla where CDs are absent, not documented, or shaped in a way that cannot be captured by the morphospace in (A). The color code is the same as in (A). Tree design adapted from [44, 45]

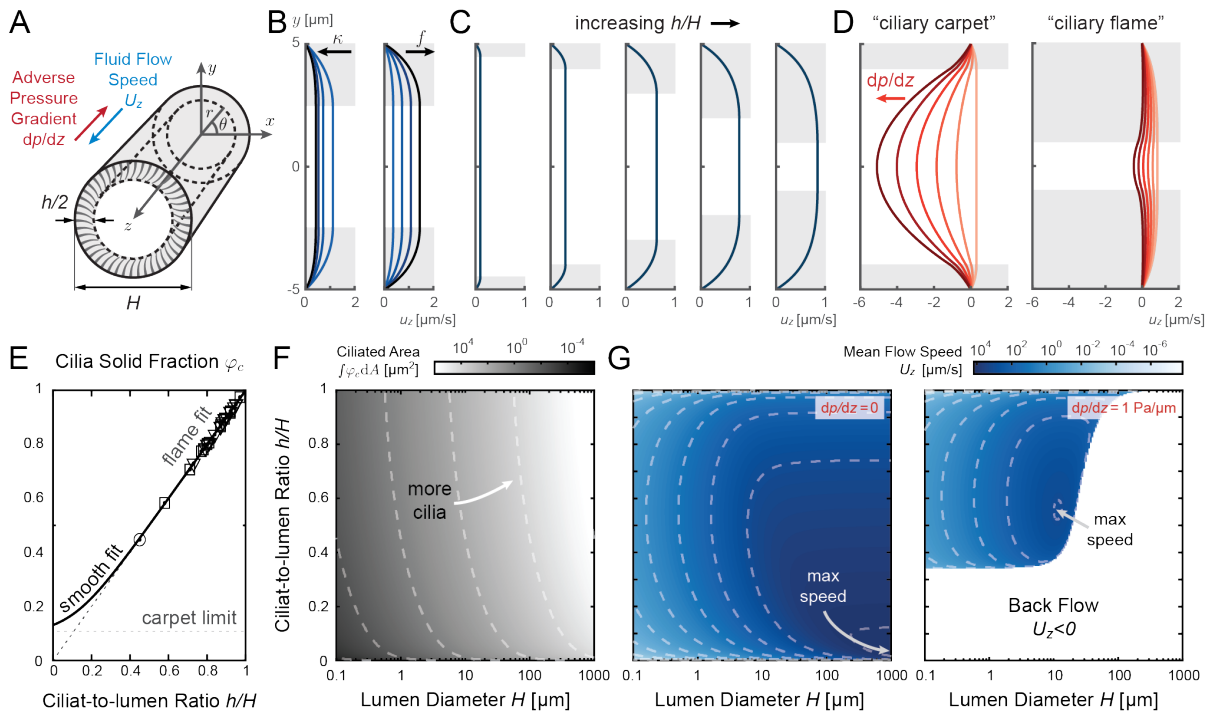

Figure 3: **Brinkman-Stokes model maps CD morphology to fluid pumping.** **A.** Schematic of axisymmetric two-layer model of ciliated duct: cilia are homogenized into an outer isotropic porous layer with specific fluid fraction φ and cilia fraction $\varphi_c = 1-\varphi$, Brinkman drag coefficient $K_c = \kappa\varphi_c$, and active force density $f_c = f\varphi\varphi_c$. **B.** The net flow u_z decreases with increasing resistance of the porous layer κ (here, $\kappa/\mu = 0.5, 1, 1.5, 2[\mu\text{m}^{-2}]$), and increases with increasing the cilia activity f (shown for $f/\mu = 0.5, 1, 1.5, 2[(\mu\text{m}\cdot\text{s})^{-1}]$). **C.** The net flow u_z approaches a bowing maximum as the cilia-to-lumen ratio h/H increases (shown for $h/H = 0.1, 0.2, 0.4, 0.6, 0.8$). **D.** Adverse pressure $\mathrm{d}p/\mathrm{d}z$ drives a backward Poiseuille flow that scales quadratically with the size of the free lumen. (shown for $\mathrm{d}p/\mathrm{d}z = 0, 0.2, 0.4, 0.6, 0.8, 1 \times 10^{-3}[Pa/um]$). Systems with small h/H (ciliary carpets) are less effective in pumping against adverse pressure compared to those with large h/H (ciliary flames). **E.** Empirical soft-plus fit of cilia fraction φ_c as a function of the cilia-to-lumen ratio h/H: ciliary flame data suggest that $\varphi_c = h/H$ for large h/H, while ciliary carpet data indicate that $\lim_{h/H\to 0} \varphi_c = 0.1$ **F.** Total ciliated area over the entire morphospace $(H, h/H)$: systems with higher H and h/H have more cilia per cross-section of the duct. **G.** Mean flow speed U_z at zero adverse pressure (left) and $\mathrm{d}p/\mathrm{d}z = 1[Pa/\mu m]$ (right). In absence of adverse pressure, systems with small h/H and large H produces the fastest flow speed. Under adverse pressure, the maximum speed occurs at a larger h/H and smaller H. Parameter values are set to: $H = 10[\mu m]$ in panels B-D with light gray background indicating the ciliary layer. $\varphi_c = 0.1$ in B-D and, in F and G, it follows from the smooth fit of E. $\kappa/\mu = 1[\mu\text{m}^{-2}]$ in C-G, $f/\mu = 1[\text{s}\cdot\mu\text{m}^{-1}]$ in C-D, $f = 15[\text{pN}\cdot\mu\text{m}^{-3}]$ in G, and $\mu = 10^{-3}[\text{Pa}\cdot\text{s}]$ throughout.

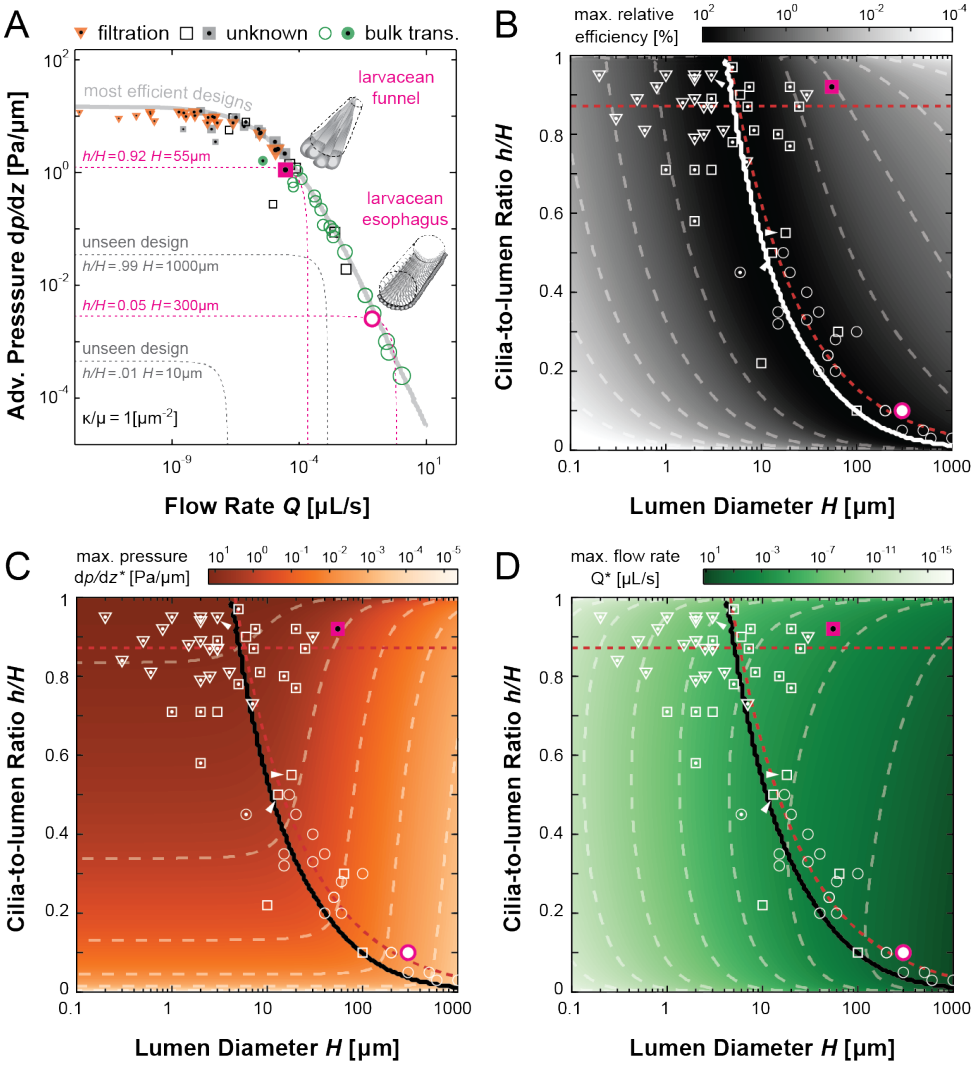

Figure 4: **Optimal CD designs. A.** Model prediction of pumping performance of optimal duct designs in the function space $(Q, \mathrm{d}p/\mathrm{d}z)$ shown in solid grey line. Non-optimal ducts (dashed grey lines) at small h/H and H generate lower pressure and flow rate, and non-optimal ducts at high h/H and H perform less than efficient while using more cilia. Biological data from Fig. 2A are superimposed. Size of the markers indicates the relative amount of ciliated area per cross section (Fig. 3F). Operating curves (dashed pink lines) of the larvacean ciliated funnel and esophagus carpet are highlighted. Our model predicts that most biological ciliated ducts operate close to the most optimal designs. **B.** Maximum relative efficiency (E_{rel} of Alg. S.1) in the $(H, h/H)$ morphospace. Most efficient designs continuously shift from carpet to flame designs. **C-D.** Maximum pressure (orange) and flow rate (green) generation in the $(H, h/H)$ morphospace. Black solid lines are the morphologies with highest relative efficiency. Red dashed lines are the power-law fits shown in Fig. 2A. $\kappa/\mu = 1[\mu\mathrm{m}^{-2}]$, $f = 15[\mathrm{pN}/\mu\mathrm{m}^3]$ with $\mu = 10^{-3}[\mathrm{Pa}\cdot\mathrm{s}]$ throughout.

Supplementary materials

Supplementary Movies

Movie S1 *In vivo* beat kinematics and flow generation by the ciliated carpet of the esophagus in the giant larvacean. Video is slowed down 2x from original speed.

Movie S2 *In vivo* beat kinematics of ciliary flame in the ciliated funnel of the giant larvacean. Note that video is slowed down 16x from original speed such that the flow moves very slowly.

Movie S3 *In vivo* beat kinematics and flow generation of the ciliary flame in the giant larvacean. Video is slowed down 8x from original speed.

S.1 Experimental Methods

S.1.1 Tissue Imaging

Live imaging of larvaceans. Four different larvacean species (*Bathochordaeus mcnutti, Bathochordaeus stygius, Fritillaria sp., Mesochordaeus erythrocephala*) were collected at water depths ranging from 55 m to 330 m in the Monterey Bay National Marine Sanctuary using acrylic detritus and suction samplers with remotely operated vehicles (ROVs) Ventana and Doc Ricketts as part of RVs Rachel Carson and Western Flyer cruises in May and October 2016, June 2018, and July 2021. Collected larvaceans were kept in seawater at 4°C for a maximum of 48 h before imaging analysis was conducted. For imaging, animals were placed in 10 cm petri dishes filled with seawater at 4°C that was regularly refreshed. The internal ciliated ducts were observed using phase contrast microscopy with 20x and 40x objectives. High-speed video microscopy was performed using either a Sony 4K Handycam FDR-AX700 or an SC1 camera (Edgertronic, CA, USA) mounted each with a custom optical adapter to the C-port or the eyepiece holder of the microscope. Ciliary beat frequency was measured from the videos using the kymograph plugin

in ImageJ [81] which visualizes the number of beat cycles per second. Metachronal wave length and direction of propagation was derived from subsequent frames in high-speed video recordings as well as spacing and slope of the stripe pattern in kymographs. Flow was visualized by adding 1 to 10 μm sized glass microspheres microspheres (Dantec Dynamics, NY, USA) and 1 to 2 μm polymer microspheres (Cospheric, CA, USA) as tracer particles to the seawater. Fluid flow velocity magnitudes were measured from particle trajectories using the Trackmate plugin in ImageJ [82]. As the high density of cilia in the larvacean ciliated duct obscured the direct imaging of tracer particles, or prevented their passage, the fluid velocity magnitude within the duct was estimated from the flux in the funnel just outside the duct.

Immunofluorescence (IF) imaging of larvaceans. Animals were fixed in 4 percent paraformaldehyde in seawater for 24 h at 4°C, then washed 3x for 10-30 min in phosphate-buffered saline (PBS) and stored in PBS at 4°C until IF staining. For IF staining, the samples were incubated with primary monoclonal antibodies against α-acetylated tubulin (to stain cilia; T6793, Sigma-Aldrich, MI, USA) in PBS for 24 h at room temperature, followed by 24 h of incubation in anti-mouse secondary antibody (Invitrogen, CA, USA), phalloidin (to stain F-actin), and DAPI (to stain nuclei) in PBS at room temperature. For IF imaging, tissues were mounted in a custom-made glass-bottom petridish and imaged with a Zeiss LSM 710 laser scanning confocal microscope using a 40x or 63x objective.

IF imaging of *Euprymna scolopes* Animals were cultured and samples were prepared and imaged using IF staining, laser scanning confocal microscopy, and transmission electron microscopy (TEM) as described previously [33].

S.1.2 Image Analysis

Measurement of duct lumen diameter and cilia-to-lumen ratio. Duct lumen (DL) diameter H and cilia-to-lumen ratio h/H were determined from own imaging data (Figs. 1, S.4 and S.1) and micrographs found in literature (Suppl. Table 1). Two different methods were used for quantitative image analysis, depending on cilia orientation (Fig. S.3A). In perpendicularly ciliated ducts, which are typically carpets (Fig. S.3B, left) and only rarely present as highly occluded ducts (Fig. S.3B, right), h/H was determined as the ciliary layer height h divided by DL diameter H. To quantify H, we identified images that showed the duct in its full width or cross-section and directly measured the diameter. To quantify h, we identified images that showed close-ups of the ciliated carpet in cross-sectional or 3D perspective and we measured cilia length. Given H and h, the cilia-to-lumen ratio h/H is determined straightforwardly. Since perpendicularly ciliated ducts are assumed to line both "floor" and "ceiling" of the ciliated lumen, h corresponds to twice the cilia length.

In longitudinally ciliated ducts, which are typically flames (Fig. S.3C, right) and only rarely feature sparsely ciliated designs (Fig. S.3C, left), the cilia are aligned longitudinally to the DL, and hence cilia density across the channel determines the cilia-to-lumen ratio, rather than cilia length. Thus, h/H was determined from the summed cross-sectional area of all cilia divided by the total cross-sectional area of the DL. For this, cross-sectional images of the duct were identified and thresholded to generate a binary image with cilia cross-sections indicated by white pixels and "empty" lumen by black pixels. Then, h/H was computed by dividing the cilia cross-sectional area (white pixels) by the total cross-sectional area of the DL (black and white pixels) and taking the square root.

Animal phyla excluded from the analysis. As indicated in Suppl. Table 1, phyla were excluded if literature suggested (1) absence of ducts with motile cilia (*e.g.*, Arthropoda, Orthonec-

tida, Placozoa, Tardigrada, Xenacoelomorpha), (2) absence of any motile cilia (*e.g.*, Nematoda, Nematomorpha), or (3) ciliated duct geometries that could not be accurately described with parameters h and H (*e.g.*, Porifera).

Classification using machine learning. We conducted machine learning using the Decision Tree function with cross-validation in the Classification Learning App in Matlab (Mathworks, MA, USA). Five morphometric parameters (duct diameter and length, cilia length and orientation, and cilia-to-lumen ratio) were used to predict bulk transport versus filtration/valve function, where known (Suppl. Table 1).

S.2 Physics-based Modeling of Ciliary Ducts

We start by solving the Stokes' equation for u_z^l in the central free lumen

$$\frac{\mu}{r}\frac{\partial}{\partial r}\left[r\frac{\partial u_z^l(r)}{\partial r}\right] = \frac{\partial p}{\partial z}, \qquad \text{for } 0 \leq r \leq a. \tag{2}$$

with finite velocity $u_z^l(0)$ at the center $r = 0$ and matching velocity at $r = a$,

$$u_z^l(a) = \varphi u_z^c(a), \tag{3}$$

where φ is the isotropic fluid fraction inside the porous layer. Here, we assumed that the downstream velocity of the solids (cilia motion averaged over beat cycles) inside the porous ciliary layer is zero at leading order, similar to the infinitesimal analysis of channel flow with passive porosity in [66]. This assumption is also consistent with the notion that f_c is the pressure gradient generated by the cycle-averaged ciliary forces pointing downstream in a confined pipe [64]. The analytical solution to Eq. (2) subject to the boundary condition in (3) is given by

$$u_z^l(r) = -\frac{\partial p}{\partial z}\frac{1}{4\mu}(a^2 - r^2) + \varphi u_z^c(a), \qquad \text{for } 0 \leq r \leq a. \tag{4}$$

The shear stress at the interface $r = a$ when approached from the free lumen side is given by

$$\sigma_{z,f}(a) = \mu \frac{\partial u_z^l}{\partial r}\bigg|_{r=a} = \frac{a}{2}\frac{\partial p}{\partial z}. \tag{5}$$

By continuity $\sigma_{z,p}(a) = \varphi \sigma_{z,f}(a)$ of shear stress $\sigma_{z,p}$ and $\sigma_{z,f}$ at $r = a$ [65, 66], we get

$$\mu \frac{\partial u_z^c}{\partial r}\bigg|_{r=a} = \varphi \frac{a}{2}\frac{\partial p}{\partial z}. \tag{6}$$

The Brinkman equation in the ciliary layer is given by

$$\frac{\mu}{r}\frac{\partial}{\partial r}\left[r\frac{\partial u_z^c(r)}{\partial r}\right] = \varphi\frac{\partial p}{\partial z} + K_c u_z^c(r) + f_c, \qquad \text{for } a \le r \le R, \tag{7}$$

subject to (6) and the no-slip boundary condition at the duct wall $u_z^c(R) = 0$. The analytical solution of (7) is given by

$$\begin{aligned} u_z^c(r) = &\left[2\left(\mathrm{I}_1(\hat{a})\mathrm{K}_0(\hat{R}) + \mathrm{K}_1(\hat{a})\mathrm{I}_0(\hat{R})\right)\right]^{-1} \\ &\left[2(\tilde{f} - \delta p)\left[\mathrm{I}_1(\hat{a})\left(\mathrm{K}_0(\hat{R}) - \mathrm{K}_0(\hat{r})\right) + \mathrm{K}_1(\hat{a})\left(\mathrm{I}_0(\hat{R}) - \mathrm{I}_0(\hat{r})\right)\right]\right. \\ &\left. - \hat{a}\delta p\left[\mathrm{I}_0(\hat{R})\mathrm{K}_0(\hat{r}) - \mathrm{I}_0(\hat{r})\mathrm{K}_0(\hat{R})\right]\right], \qquad \text{for } a \le r \le R, \end{aligned} \tag{8}$$

where $\hat{(\cdot)} = \sqrt{\frac{K_c}{\mu}}(\cdot)$, $\delta p = \frac{\varphi}{K_c}\frac{\partial p}{\partial z}$, $\tilde{f} = \frac{f_c}{K_c}$, and $\mathrm{I}_{(\cdot)}, \mathrm{K}_{(\cdot)}$ are modified Bessel functions of order $(\cdot)$.

Note that since Equation (8) is linear in δp and $\tilde{f}$, we only need to compute solution $U_c = u_z(\tilde{f} = 1, \delta p = 0)$ and $U_p = u_z(\tilde{f} = 0, \delta p = 1)$ and obtain $u_z(\tilde{f}, \delta p) = \tilde{f}U_c + \delta p U_p$.

It is interesting to note that for $\partial p/\partial z = 0$, u_z becomes independent of a as $R \to \infty$. In other words, at zero adverse pressure, the cilia driven flow speed becomes independent of h/H for large H. This trend dictates the existence of an optimal efficiency at small adverse pressure because the amount of active material increases with higher h/H.

S.3 Effective parameter selection

Setting lower limit of the cilia solid fraction φ_c in the ciliary carpet layer. We seek an estimate of the cilia solid fraction φ_c within the ciliary carpet layer. Since the cilium diameter and inter-cilium spacing are roughly equal (about 0.2 μm), in a uniformly-covered ciliated tissue, the expected cilia density should be about $\varphi_c = 0.5^2 \equiv 25\%$. However, many ciliary carpets contain both ciliated and non-ciliated cells, such that the tissue-level coverage fraction of ciliated cells is much less than 100%. In mouse trachea, the ciliated cell coverage can be as low as 37% [13], and amphibian ciliated skin exhibits a 50% ciliated cell coverage [83]. Additionally, individual ciliated cells can have partial ciliation, such as in ependymal epithelia in mammalian brain ventricles where the ciliated area overall approaches only 32% of total surface [84, Fig. 3]. Thus, the overall cilia density, accounting for this heterogeneity in surface coverage is far less than 25%. For example, a tissue with 30%–50% coverage fraction, at 25% cilia density within the covered patches would have an overall cilia density of about 7.5%–12.5%. Thus, we used $\varphi_c = 10\%$ as a lower bound for our cilia solid fraction (see Fig. 3E of the main text).

Setting dimensional scale of the active force density f. To calibrate the correct order of magnitude for f, we used measurements of pumping performance in the ciliary flames that connect the peritoneal cavity to the vasculature and filter lymphatic in the toad *Bufo marinus* and *Bufo bufo* [85, 86]. This filtration system consists of 600–800 ciliated flames. Flames exhibit circular and elliptical apertures between 7–40 μm in diameter [85]. Although openings as large as 100 μm were reported, many larger flames appeared to have flap covers that would reduce their "hydrodynamic" diameter [85, Fig.4]. No clear length was visible or reported in [85], but similar ciliary flames have lengths of at least 30 μm [86, Fig. 7c]. By measuring the pressure difference between the peritoneal and the blood compartment, the authors of [85] reported a maximum flow rate of 0.5±0.03 ml/hr, a flow rate of 0.17 ml/hr at about 200 Pa, and

a maximum pressure of 310 ± 20 Pa (see [85, Fig. 12]). A summary of these measurements is given in Table S.1. As a side note, in our survey of ciliated organs in Fig. 2 of the main text, we used a specific *Bufo marinus* funnel of $H = 7$ μm and $h/H = 0.73$ shown in [85, Fig.11] due to its clear visualization of cilia density. To calibrate our model and estimate the force density, we considered in the context of our model the specific example of a ciliated flame of average lumen diameter 15 μm and length 100 μm. We used the measured cilia-to-lumen ratio of $h/H = 0.73$ and the parameter values $\kappa/\mu = 1$ μm^{-2} and $\mu = 10^{-3}$ Pa·s corresponding to the viscosity of water. Our model predicted that this funnel matches the maximum pressure of about 300 Pa observed in [85] if we set the active force density to $f = 15$ pN/μm^3. This value is well within the mechanical capability of cilia averaged over a stroke cycle, given that the internal motors of a single respiratory cilium can generate about 60 pN of force during its effective stroke at the tip, implying a force density of nearly 200 pN/μm^3 for a 200 nm wide, 10 μm long cilium [87]. To further verify the validity of the estimate of $f = 15$ pN/μm^3 for flames of dimensions 100 μm $\times$ 15 μm and $h/H = 0.73$, we calculated that a total of 800 such flames produce a flow rate of about 0.16 ml/hr against 200 Pa of pressure with a maximum attainable flow rate of about 0.46 ml/hr, which are very close to the experimentally reported flow rates. A comparison of experimental data and our model predictions are available in Table. S.1.

Effect of changing the effective Brinkman coefficient $K_c = \kappa\varphi_c$. Since the Brinkman drag coefficient is fundamentally empirical for geometrically complex systems [88, 89], we assumed for simplicity that κ is of the same order as the fluid viscosity throughout the main text of our study. However, since $\sqrt{\mu/\kappa}$ can also be interpreted as an effective pore size for the porous layer [90], it is interesting to see how changing κ would affect the results of our optimization. In Fig. S.7, we show that increasing the relative value of κ/μ (decreasing the effective pore size) decreases the lumen diameters that maximize the pumping efficiency E. Importantly, all values

of κ produce the same relationship between the value of adverse pressure gradient $\mathrm{d}p/\mathrm{d}z$ and cilia-to-lumen ratio h/H, implying that different values of κ would only move the most efficient designs (solid white lines in Fig. 4B or solid black lines in Fig. 4C-D) laterally in the $(H, h/H)$ morphospace (see Fig. S.7B). This effect could explain why some of the biological ciliated ducts deviates laterally from the most efficient line obtained for the value $\kappa/\mu = 1[\mu m^{-2}]$; they could be more efficient for a different value of effective pore size.

S.4 Quantitative comparison of excretory organs

Flame cells serve as a basic filtration unit in many mm-scale organisms, but are markedly absent in larger organisms, (except during some stages of development) [71]. Filtration in larger organisms, the human kidney for example, leverages the blood pressure generated by a muscular heart. We propose that the lack of filtration by ciliary flames in larger animals might be (partly) due to the unfavorable scaling of pressure and flow generation in flame-based filtration compared to blood pressure-based filtration, as the following example illustrates. In humans, the filtration pressure provided by the capillary blood pressure is on the order of $5 - 10$ kPa [91]. The average filtration rate of the kidney is ca. 180 liters of blood per day, which, considering nearly 1,000,000 filtration units (glomeruli) [92], indicates a filtration rate of 7.5 μl/hr per glomerulus. Given an average glomerular volume of $6 \cdot 10^6$ μm^3, the total space taken up by the filtration units is ca. 6 ml [92]. The larvacean's ciliated funnel, the largest ciliary pump found in our survey, can efficiently pump 0.4 μl/hr of fluid against 0.6 Pa/μm of pressure gradient (Fig. 4A). This means that the parallel operation of ca. 20 such funnels, each with more than 8 mm in length, can produce comparable a flow rate (20$\times$0.4 = 8 μl/hr) at the minimum 5 kPa pressure drop observed across the glomerular filtration barrier. Assuming biologically feasible, such funnel would be able to sustain a maximum pressure at nearly 10 kPa without flow. Using the lumen diameter $H = 55$ μm as a lower bound, the resulting tissue volume that

replaces a single glomerulus would measure 0.02 μl, which leads to about 0.4 liters if these funnels were to replace the operation of all 6 ml of glomerular volume in an entire kidney. This example demonstrates the unfavorable scaling of cilia-based filtration to larger body sizes and their higher filtration rate demands.

References

81. Abràmoff, M. D., Magalhães, P. J. & Ram, S. J. Image processing with ImageJ. *Biophotonics international* **11,** 36–42 (2004).
82. Tinevez, J.-Y. *et al.* TrackMate: An open and extensible platform for single-particle tracking. *Methods* **115,** 80–90 (2017).
83. Boselli, F., Jullien, J., Lauga, E. & Goldstein, R. E. Fluid mechanics of mosaic ciliated tissues. *Physical review letters* **127,** 198102 (2021).
84. Mirzadeh, Z., Han, Y.-G., Soriano-Navarro, M., Garcıa-Verdugo, J. M. & Alvarez-Buylla, A. Cilia organize ependymal planar polarity. *The Journal of Neuroscience* **30,** 2600–2610 (2010).
85. Morris, J. L. Structure and function of ciliated peritoneal funnels in the toad kidney (Bufo marinus). *Cell and Tissue Research* **217,** 599–610 (1981).
86. Møbjerg, N., Larsen, E. H. & Jespersen, Å. Morphology of the nephron in the mesonephros of Bufo bufo (Amphibia, Anura, Bufonidae). *Acta Zoologica* **79,** 31–50 (1998).
87. Hill, D. B. *et al.* Force generation and dynamics of individual cilia under external loading. *Biophysical journal* **98,** 57–66 (2010).
88. Nield, D. The Beavers–Joseph boundary condition and related matters: a historical and critical note. *Transport in porous media* **78,** 537–540 (2009).
89. Nield, D. & Kuznetsov, A. An historical and topical note on convection in porous media. *Journal of Heat Transfer* **135,** 061201 (2013).
90. Alvarado, J., Comtet, J., De Langre, E. & Hosoi, A. Nonlinear flow response of soft hair beds. *Nature Physics* **13,** 1014–1019 (2017).
91. Rubenstein, D., Yin, W. & Frame, M. D. *Biofluid Mechanics: an Introduction to Fluid Mechanics, Macrocirculation, and Microcirculation* (Academic Press, 2015).
92. Nyengaard, J. & Bendtsen, T. Glomerular number and size in relation to age, kidney weight, and body surface in normal man. *The Anatomical Record* **232,** 194–201 (1992).
93. Webber, J. B. W. A bi-symmetric log transformation for wide-range data. *Measurement Science and Technology* **24,** 027001 (2012).

Algorithm S.1 Evaluating performance of duct designs on the morphospace $(H, h/H)$ and identifying optimal duct designs that maximize efficiency E under adverse pressure.

Require: list of CD morphological parameters:
$(H, h/H)$ // morphospace formed by lumen diameters and cilia-to-lumen ratios
$\mu, f, \varphi_c(H, h/H)$ // fix viscosity, active force scale and forms for cilia solid fraction.

for $\kappa/\mu = 0.1, 1, 10$ **do**
  Pre-compute the following and store each as a matrix over the morphospace $(H, h/H)$:
    $U_c \equiv U_z(H, h/H)$ for $f = 1, \mathrm{d}p/\mathrm{d}z = 0$ // flow velocity due to unit cilia activity
    $U_p \equiv U_z(H, h/H)$ for $f = 0, \mathrm{d}p/\mathrm{d}z = 1$ // flow driven by unit adverse pressure
    $A_c \equiv \frac{1}{4}\pi\varphi_c H^2(1 - (1 - h/H)^2)$ // total ciliated area per cross section
  Compute maximum possible pressure and flow rate generation over $(H, h/H)$:
  $Q^* \equiv \frac{1}{4}\pi H^2 U_c$ // Maximum flow rate occurs when adverse pressure is absent.
  $\mathrm{d}p/\mathrm{d}z^* \equiv -f \cdot U_c/U_p$ // Maximum pressure is generated when net flow is zero.
  Initialize null relative efficiency score over the entire morphospace $(H, h/H)$:
    $E_{\text{rel}} \equiv$ **zeros**$(H, h/H)$
  for $\mathrm{d}p/\mathrm{d}z = 10^{-10}, \ldots, 10^2$[Pa/$\mu$m] **do**
    $U = f \cdot U_c + \mathrm{d}p/\mathrm{d}z \cdot U_p$ // Compute average flow speed at given adverse pressure.
    if max$(U) < 0$ **then**
      break // Quit if no design parameters can pump at this $\mathrm{d}p/\mathrm{d}z$.
    $E = Q/A_c = \frac{1}{4}\pi H^2 U/A_c$ // Compute efficiency at given adverse pressure.
    Identify optimal designs at given $\mathrm{d}p/\mathrm{d}z$:
      $[E^\dagger, (H, h/H)^\dagger] =$ **max**(E) // Find design parameters that maximize efficiency
      $E_{\text{rel}} =$ **max**$(E_{\text{rel}}, E/E^\dagger)$ // Accumulate relative efficiency score
      return $(H, h/H)^\dagger$ // Return optimal design parameters as function of $\mathrm{d}p/\mathrm{d}z$.
  return $Q^*, \mathrm{d}p/\mathrm{d}z^*, E_{\text{rel}}$ // Return quantities as function of κ/μ.

Filter Type (organism)	Sustainable Pressure [kPa]	Total Filtration Rate [mL/hr]	Unit Size (L x Ø) [μm]	Unit Volume [μL]	Number of Units Required	Total Volume [μL]
Blood-pressure-based Filter (Human kidney glomeruli)	5 – 10	7500	N/A	0.006	1,000,000	6,000
Cilia-powered Filter (*B. marinus* peritoneal flame)	0.29 – 0.33	0.17 @ 200 Pa	unknown x 7 – 40	unknown	600 – 800	unknown
Cilia-powered Filter (simulated)	0.3	0.16 @ 200 Pa	100 x 15	0.00002	800	0.01
Larvacean Ciliated Funnel (*Bathochordaeus sp.*)	0.2	0.4 @ 100 Pa	160 x 55	0.0004	N/A	N/A
Cilia-powered "human kidney"	10	7500 @ 5 kPa	8000 x 55	0.02	20,000,000	400,000

Table S.1: **Pumping characteristics of observed and simulated filtration systems.** We list the structural and functional parameters found in literature (black) and derived based on our model (blue). Data for human kidney glomeruli are approximated from [91, 92]. Data from the cilia powered peritoneal filtration in *Bufo marinus* are based on [85]. In all simulations, we used $f = 15$ pN/μm^3, $\kappa/\mu = 1$ μm^{-2}, and $\mu = 10^{-3}$ Pa·s.

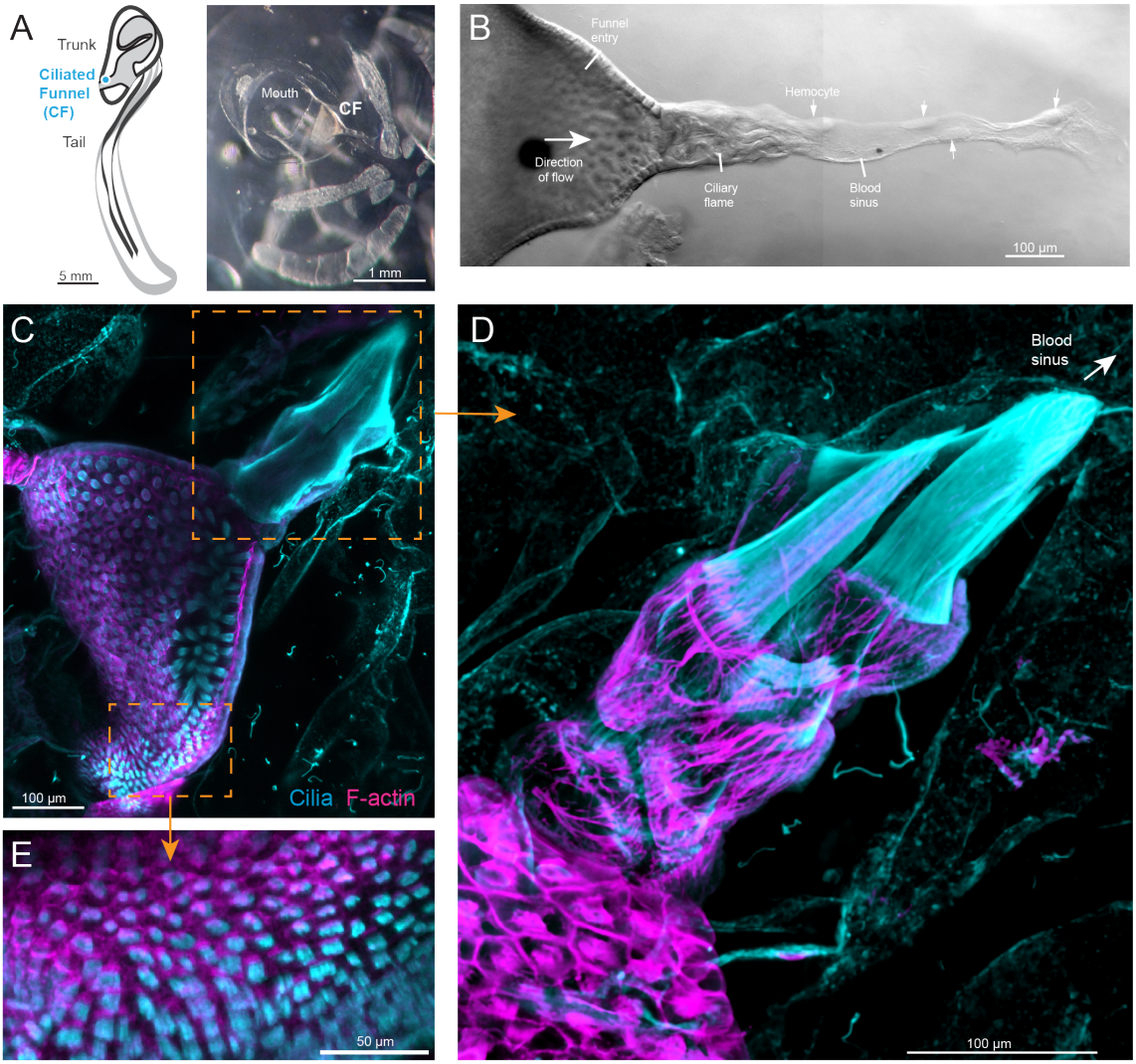

Figure S.1: **The flow generated by the ciliary flame of the giant larvacean appears to draw ambient seawater through a lattice of non-motile cilia, through the ciliary flame, and into the blood sinus.** **A**, The ciliated funnel (CF) in the giant larvacean *B.stygius* branches off the mouth cavity (M). **B**, Phase-contrast cross-section of entire ciliated funnel shows protective lattice of non-motile cilia in the funnel entry (opening to mouth cavity), ciliary flame, and connection to blood sinus with putative hemocytes (small arrows). The direction of the cilia-driven flow is inwards (large arrow), consistent with a multi-stage filtration system [68]. **C**, Cross-sectional confocal image of the ciliated funnel in *B.stygius* including the funnel entry and the ciliary flame. **D**, Close-up on the ciliary flame, showing an actin mesh (magenta) encasing the large ciliary flame (cyan) which is composed of multiple, tightly packed ciliary flame cells and connects to the blood sinus. **E**, Close-up on the lattice of non-motile cilia that project into the funnel entry.

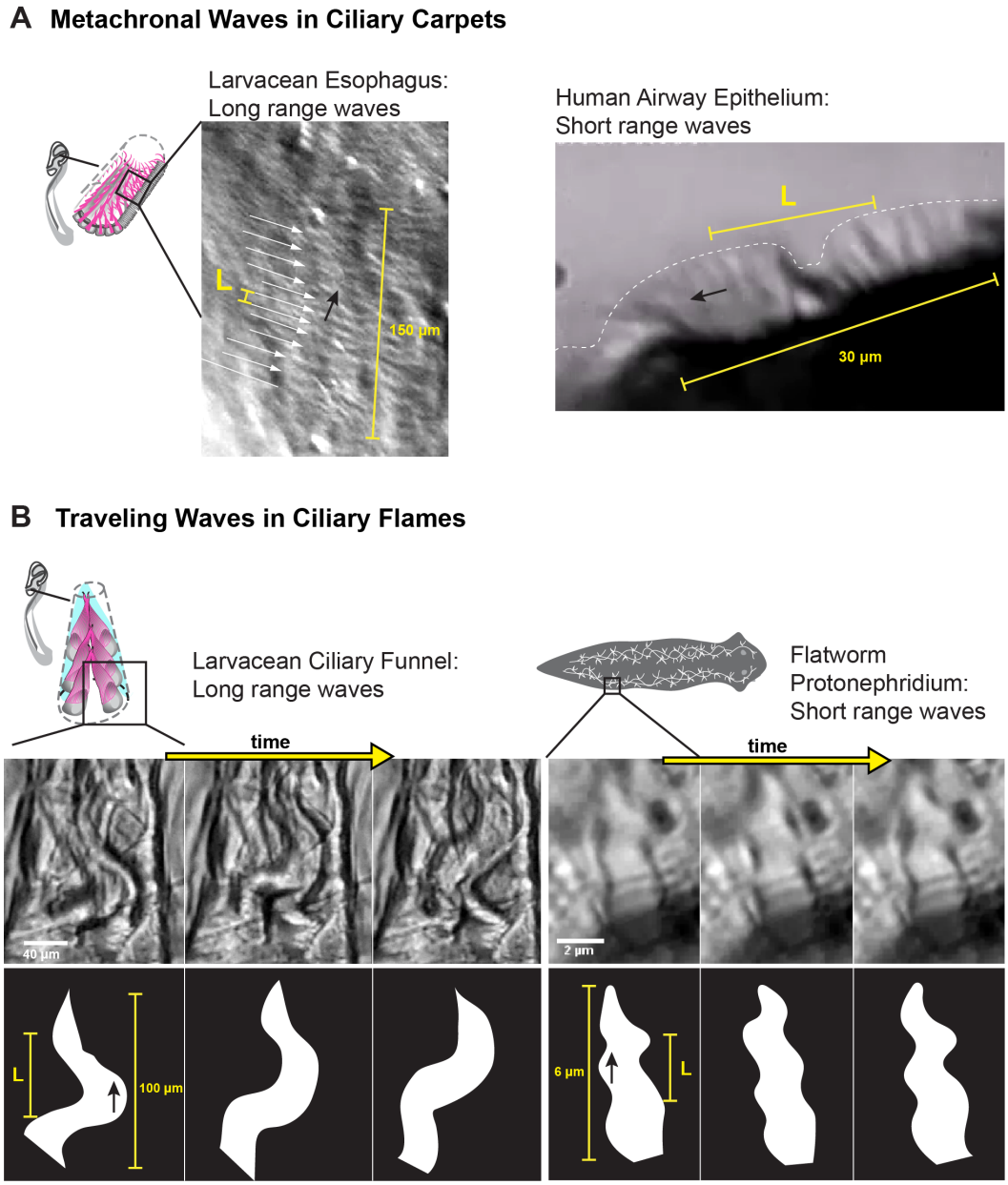

Figure S.2: **Ciliary beat coordination in metachronal and traveling waves.** **A**, Ciliary carpets generate long-range or short-range metachronal waves of ciliary beat. Left, larvacean esophagus, arrows indicate crests of metachronal wave; right, engineered human airway epithelium. L, metachronal wave length. **B**, Ciliary flames generate long-range or short-range metachronal waves of ciliary beat. Left, time lapse of wave traveling along flame of larvacean ciliary funnel; right, time lapse of wave traveling along flame of planarian (flatworm) protonephridium. L, traveling wave length.

A Measuring ciliary fraction h/H in different design

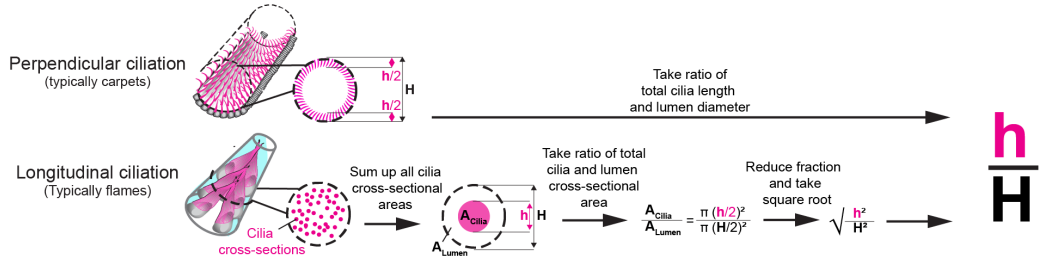

B Example analyses for perpendicular cilia

Example 1: h/H ~ 0 (*Carpet design*)

Ciliated esophagus in the Giant Larvacean *Bathochordaeus stygius* (Urochordata)

1. Use imaging data that reveals duct geometry (Here: maximal projection of confocal microscopy optical sections) and measure lumen diameter H.

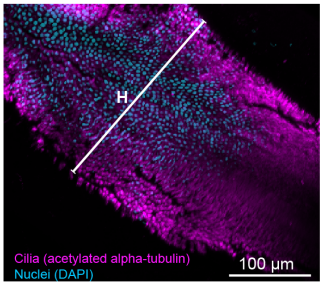

2. Use imaging data that reveals cilia length (Here: orthogonal projection of confocal microscopy optical sections) and measure cilia length (1/2 h).

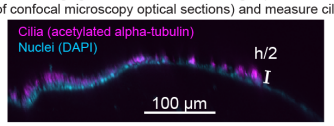

3. Compute the cilia-to-lumen ratio h/H:

$$h/H = \frac{\text{2 x Length of cilia}}{\text{Lumen diameter}} = 0.1$$

Example 2: h/H ~ 1

Bottleneck of the ciliated duct in the light organ of the Hawaiian bobtail squid *Euprymna scolopes* (Mollusca)

1. Use imaging data that reveals duct geometry (Here: maximal projection of confocal microscopy optical sections) and measure lumen diameter H.

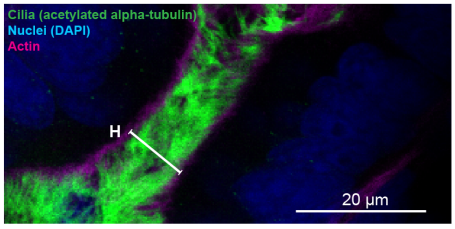

2. Use imaging data that reveals cilia length (Here: confocal microscopy optical section) and measure cilia length (1/2 h).

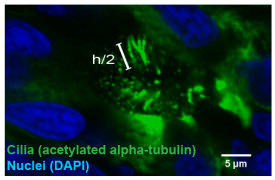

3. Compute the cilia-to-lumen ratio h/H:

$$h/H = \frac{\text{2 x Length of cilia}}{\text{Lumen diameter}} = 0.9$$

C Example analyses for longitudinal cilia

Example 1: h/H ~ 0

Distal collecting duct of protonephridia in *Artioposthia sp.* (Platyhelminthes) 1. Use cross-sectional image of duct that reveal cilia and lumen diameter H. (Here: TEM image reproduced under Creative Commons CC BY license from Poddubnaya et al.,Parasites & Vectors, 2020)

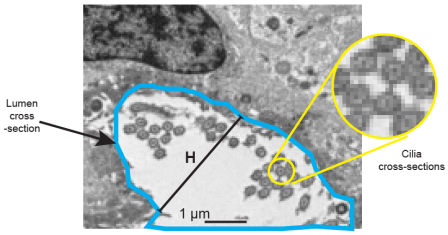

2. Mask duct to isolate ciliated lumen (left) and threshold pixel intensity to obtain a binary image (left) combining all cross-sectional areas of cilia in white and "empty" lumen space in black.

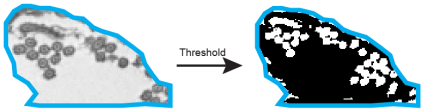

3. Compute the cilia-to-lumen ratio h/H:

$$h/H = \sqrt{\frac{\text{Cross-sectional area of cilia}}{\text{Cross-sectional area of lumen}}} = \sqrt{\frac{A_{Cilia}}{A_{Lumen}}} = 0.2$$

Example 2: h/H ~ 1 (*Flame design*)

Ciliated funnel in the Larvacean *Oikopleura dioica* (Urochordata)

1. Use cross-sectional image of duct that reveal cilia and lumen diameter H (Here: TEM image reproduced with permission from Holmberg, Acta Zoologica, 1982)

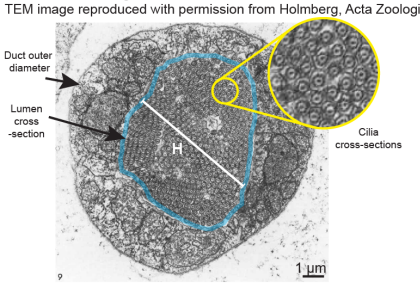

2. Mask duct to isolate ciliated lumen (left) and threshold pixel intensity to obtain a binary image (left) combining all cross-sectional areas of cilia in white and "empty" lumen space in black.

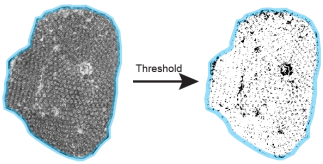

3. Compute the cilia-to-lumen ratio h/H:

$$h/H = \sqrt{\frac{\text{Cross-sectional area of cilia}}{\text{Cross-sectional area of lumen}}} = \sqrt{\frac{A_{Cilia}}{A_{Lumen}}} = 0.9$$

Figure S.3: **Methods to measure duct lumen (DL) diameter and cilia-to-lumen ratio**. **A**,In carpet-style ciliated ducts h/H was determined as the ratio of the ciliary layer height h and the duct lumen diameter H. Since ciliary carpets are assumed to line both "floor"and "ceiling" of the ciliated duct, ciliary length corresponds to 1/2 h. In flame-style ciliated ducts the cilia are aligned longitudinally to the duct and hence cilia density rather than length determines the cilia-to-lumen ratio. h/H was therefore determined as the square root of the ratio of the cross-sectional area of the cilia to the cross-sectional area of the duct lumen. **B**, Example analyses of carpet designs with low h/H and high h/H values (own data). **C**, Example analyses of flame designs with low h/H and high h/H values. The left TEM image was reproduced from Poddubnaya, L.G., et al., Parasites Vectors 13, 442 (2020), under Creative Commons CC BY license. The right TEM image was reproduced from Holmberg K, Acta Zoologica 63.2 (1982): 101-109, with permission from John Wiley and Sons.

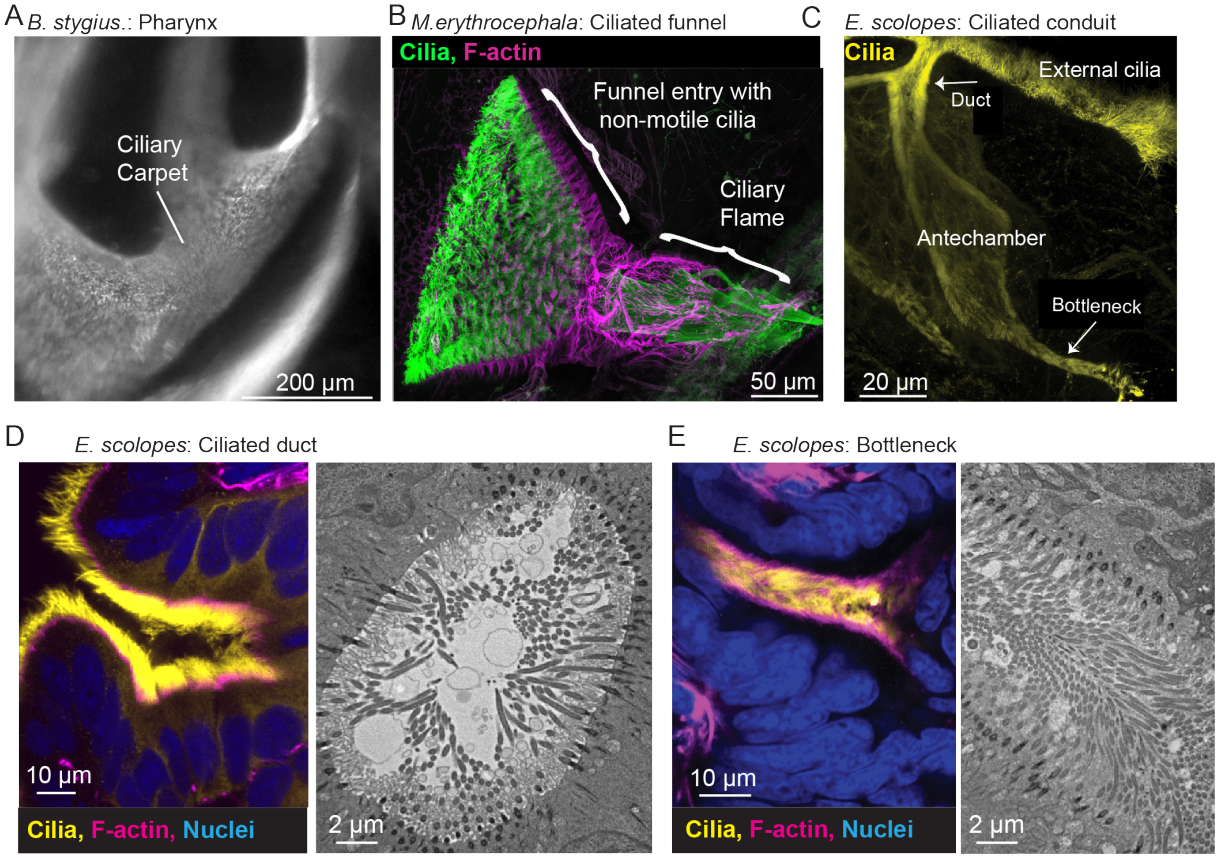

Figure S.4: **Carpet and flame-type ciliated ducts in Urochordates and Mollusks analysed in this study**. **A**, The ciliated pharnyx in larvaceans, here *B. stygius* (Urochordata), is characterized by a ciliary carpet and a low h/H ratio. **B**, The ciliated funnel in larvaceans, here *Mesochordaeus erythrocephala* (Urochordata), is a flame design. **C**, The ciliated conduit of the light organ in the Hawaiian Bobtail Squid *Euprymna scolopes* (Mollusca) features a carpet design in the duct and antechamber regions and a flame-like design in the bottleneck region, as seen in the close-up immunofluorescent and transmission electrode images of **D**, the ciliated duct and **E**, the bottleneck region.

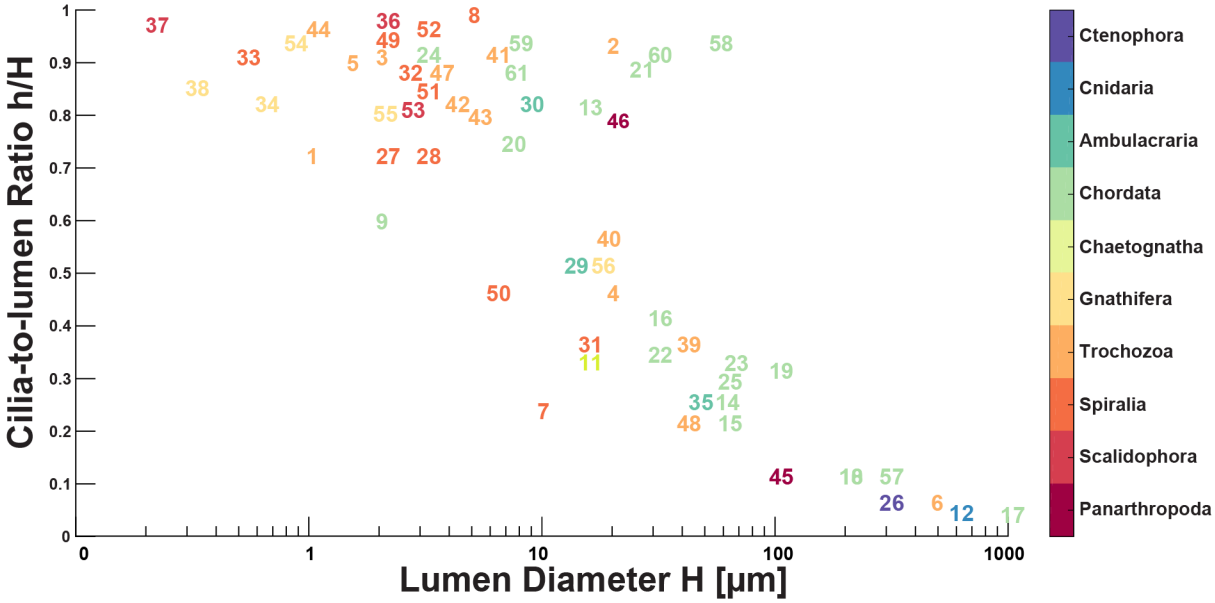

Figure S.5: **Indexed plot of cilia-to-lumen ratio as a function of lumen diameter**. The plotted numbers correspond to the index numbers in Suppl. Table 1 and hence indicate the animal species corresponding to each data point, as well as the associated source of the data.

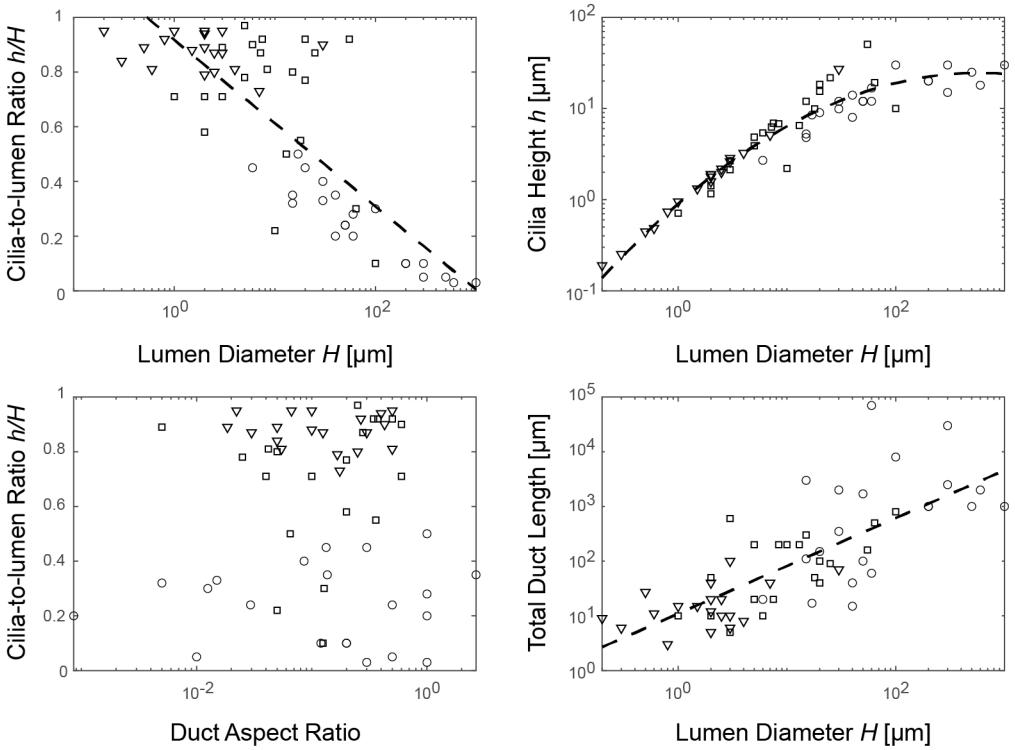

Figure S.6: **Fits of measured geometric parameters.** We show the fitted trend of cilia-to-lumen ratio h/H vs lumen diameter H in log-linear scale (linear fit), cilia "height" h (not literal length of cilia for flame designs) and lumen diameter H in log-log scale (quadratic fit), and total duct length vs lumen diameter H in log-log scale (linear fit). On the other hand, h/H and duct aspect ratio of diameter H over total duct length shows no clear correlation. Here the symbols follow that of Fig. 2: ○ for CDs with confirmed transport/mixing function, ▽ for filtration, and □ for unknown function.

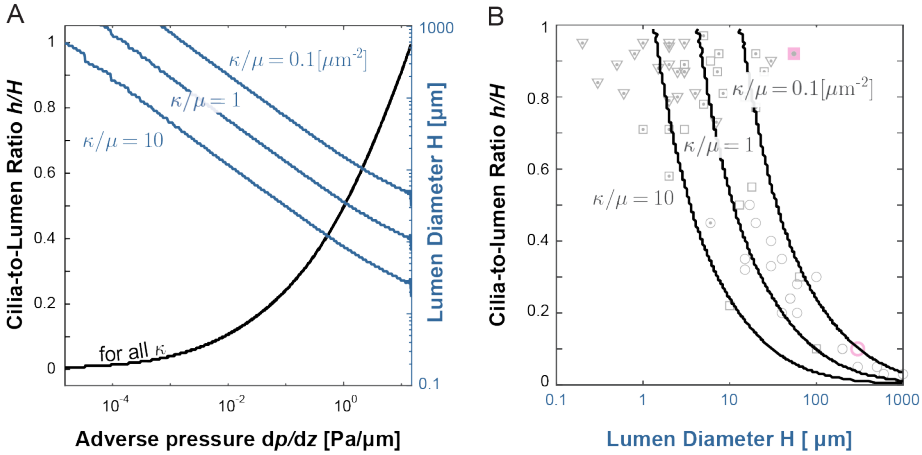

Figure S.7: **Effect of Brinkman coefficient κ on morphology of most efficient designs. A.** Result of our optimization (Algorithm S.1) for different values of κ while maintaining all other parameters fixed. The most efficient designs have smaller lumen diameter H at a higher hydraulic resistance coefficient κ/μ, but the optimal cilia-to-lumen ratio h/H do not change. **B.** In morphospace, the most efficient designs shift only horizontally for different values of κ. This provides an additional explanation for the lateral spread of the biological data points. Here we used $\mu = 10^{-3}$[Pa· s] and $f = 15$[pN/μ m^3].